Finite element framework for modeling conducto-radiative transfers within heterogeneous media at both discrete and continuous scales

Salih Ouchtout, Benoit Rousseau, Y. Favennec

Finite element framework for modeling conducto-radiative transfers within heterogeneous media at both discrete and continuous scales

S. Ouchtout, B. Rousseau, Y. Favennec*

Nantes Université, CNRS, Laboratoire de thermique et énergie de Nantes, LTeN, UMR 6607, F-44000 Nantes, France

Abstract

The paper compares three distinct conducto-radiative models that can be used for modeling heat transfer at high temperature in view of being integrated within a topology optimization process. Finite elements are extensively used. Non-linearities are handled using a fixed-point method coupled with a Newton–Raphson linearization method. A three-dimensional square lattice is sandwiched between a hot and a cold plate. The discrete mesoscopic scale is the reference model. At all conduction-to-radiation regimes, and even when radiation predominates, it appears that the continuous-scale approach, which has been set-up thanks to proper homogenization laws, gives satisfactory results, which is not the case for the Rosseland approximation model. The homogenized continuous-scale model appears to be a good candidate for being used in the future in topology optimization problems.

Keywords: conductive-radiative transfer, continuous-scale approach, discrete-scale approach, open-cell foams, Newton-Raphson, finite elements, parallel computing

1. Introduction

In the field of free-carbon heat generation and waste heat recovery at high temperatures ($T > 1000$ °C), there is a growing interest in the design of durable high temperature energy systems with high thermal efficiency such as gas-to-gas heat exchangers [1], volumetric solar receivers [2, 3, 4], thermal protection systems [5, 6, 7, 8], and radiant tube inserts [9], among other interesting processes. These systems can be described as radiative-convective heat exchangers [10] containing porous structures which play a key role in promoting the volumetric propagation of both radiation and temperature advected by a fluid flow. In reason of their textural and chemical features, refractory macroporous ceramics such as open-cell foams [11] and media with porosity-gradient structures [9]) know an increasing concern. Indeed, for engineering applications such as heat exchangers working at high-temperature, they present interesting performances in terms of energy conversion. When convective transfer can be neglected, which is the case for stagnant fluids, a global comprehension of both conductive and radiative transfers taking place within the porous medium structure can allow one to design them smartly, in order to best satisfy a pre-established objective.

The main perspective induced by the presented work is the design of architectured materials, and, in particular, lattice materials. These materials are becoming increasingly popular in the context of additive manufacturing. To achieve this goal, we exploit a numerical tool we have developed these last years: a fast and accurate finite element solver dedicated to the solution of the radiative transfer equation. This solver, which is based on stabilized vectorial finite elements [12, 13], has been parallelized [14] in such a way that the calculation can run on multiple processes. Further, its matrix-free version highly reduces the memory load on each process, so that complex geometries can be dealt with [15]. This solver, which uses efficient matrix solvers and preconditioners [16], takes into account several kinds of radiative boundary conditions such as incoming collimated radiative intensity, emission, and specular reflexions [17]. The solver is also able to design ad hoc angular discretization [18].

Macroporous ceramics have two phases, one is solid and the other is fluid. A fine modeling of heat transfers taking place in this two-phases medium should be made, ideally, at the scale of the discretized material, i.e. at the pore scale. If the solid phase is considered as an absorbing medium, the conductive problem is to be solved within the solid phase, the radiative problem is to be solved solved within the fluid phase, which can be considered as vacuum, and the energy transfer between the two problems takes place at the solid-void interface separating apart both phases. Such a discrete-scale approach, finely described in a previous work [19], makes it possible to achieve a good level of details in terms of three-dimensional temperature fields, conductive flux fields, and radiative flux fields. This is important because, at high temperature, heat transfer modes are coupled in

*Corresponding author: yann.favennec@univ-nantes.fr

such a way that a given heat transfer mode is affected by the other modes, making their effective contribution non linear [20].

In order to apply the homogenization methodology, the study considered here deals with the computation of coupled conducto-radiative heat transfer problems involving high temperature in a three-dimensional square lattice, using a single cell as well as multiple cells, at both the discrete mesoscopic scale and at the related continuous macroscopic scale. Along with this simple geometry, a highly simple physical situation is dealt with, where the considered domain is sandwiched in between a hot plate and a cold plate. The main goal of the study is to evaluate, in such a simple situation, the amount of errors one gets, in terms of temperature, using the coupled model at the macroscopic continuous scale respectively to the reference discrete-scale model at the mesoscopic level. Added to the continuous-scale model, the Rosseland approximation, which assumes that the porous medium is considered optically thick [21], is also compared to the discrete-scale model to get a clear idea on approximated models which could be used in future optimization processes, knowing the bias and errors associated to them.

In this study, three models are presented for coupled conducto-radiative problems at mesoscopic and macroscopic scales. One is the discrete-scale coupled model, presented above. Another is the related continuous-scale coupled model. The last one is the Rosseland approximation model. The passage from all of them is detailed in the paper. Conducto-radiative problems being non linear, an iterative scheme is to be set-up in order to make the solution to converge. We propose an iterative scheme based on a weak coupling between both the radiative transfer equation and the heat conduction equation and, in order to improve drastically the convergence, the Newton–Raphson iterative method is derived on the non-linear heat conduction equation.

The paper is organized as follows. Section 2 details the three considered conducto-radiative models. Section 3 details the solution process thanks to finite elements for conduction problems, and vectorial finite elements for the radiative transfer equation. This section also details iterative schemes such as the fixed-point method and especially the Newton–Raphson linearization process. Section 4 is dedicated to the global set-up, with useful non-dimensional numbers, geometry definition, and other necessary tools used for validations, convergence analysis, and comparisons between models. Section 5 details and discusses the numerical results of the three presented models. It firstly presents the numerical results related to the continuous-scale coupled model, with validation and convergence analysis. This section then presents the numerical results related to the Rosseland model, with a comparison respectively to the continuous-scale coupled model, and a convergence analysis. It finally presents the numerical results related to the discrete-scale coupled model, with a comparison respectively to the continuous-scale coupled models, and, again, a convergence analysis. The conclusion which can be drawn from numerical results is twofold. At first, a numerical process has been designed to solve efficiently coupled conducto-radiative problems at high temperature, at both the discrete and continuous scales. The models have been validated thanks to data from the literature. Second, if effective properties are carefully calculated, the continuous-scale coupled model approximates the discrete-scale coupled model with moderate errors of maximum 5 %. The corollary of this is that the continuous-scale coupled model could be the one used in the future in optimization processes when coupled with the homogenization methodology.

2. Models of conducto-radiative transfers

Heat transfer involved in macroporous media at high temperature may include the three modes of heat transfer, namely conduction, convection, and radiation. The balance between these modes is influenced by operating conditions as well by textural parameters such as porosity or ligament size, and also physical properties, such as thermal conductivity, scattering coefficient, etc. At high temperature, heat transfer modes may be coupled so that, for example, the global heat flux is not as simple as the summation of individual fluxes [20, 19]. The knowledge of individual contributions as well as their coupling effect is a crucial route for optimizing processes involving high temperature, modifying adequately space-dependent physical properties at macro-scale, or unitary cells at meso-scale. Among the three heat transfer modes, only the conduction and radiation are considered in the study; fluid flows contribution shall be taken care of in a forthcoming study. Further, in this paper, three distinct conducto-radiative models are considered:

i) the discrete-scale coupled model (DS-CM) in which two phases are considered, namely the void phase in which radiation occurs, and the solid phase in which conduction occurs. The transfer between these two physics takes place on the internal boundary between both domains;
ii) the continuous-scale coupled model (CS-CM) that couples both physics of radiation and conduction within a single domain. The physical properties are effective ones calculated both from the ones of the discrete-scale model and from the geometry itself (porosity, pore size, etc.);
iii) the related Rosseland approximation model (RM) that combines both physics of radiation and conduction in a single non-linear conduction equation.

The considered physics deals with a medium located between two plates on which a given temperature is prescribed; on all other boundaries, a symmetry is considered.

2.1. The discrete-scale coupled model (DS-CM)

In the discrete-scale coupled model, the solid phase domain is fully embedded within a box. This box, without the solid phase, is the void phase. The solid phase is denoted as $\Omega_\mathrm{s} \subset \mathbb{R}^3$, and the void phase is denoted as $\Omega_\mathrm{v} \subset \mathbb{R}^3$. The union of these two domains yields the whole domain treated in the previous section, i.e. $\Omega_\mathrm{s} \cup \Omega_\mathrm{v} := \Omega$. Further, the solid (resp. void) phase boundary is denoted $\partial\Omega_\mathrm{s}$ (resp. $\partial\Omega_\mathrm{v}$). The solid–void interface is denoted $\Gamma = \partial\Omega_\mathrm{s} \cap \partial\Omega_\mathrm{v}$. Also, let $\boldsymbol{n}_\mathrm{s}$ (resp. $\boldsymbol{n}_\mathrm{v}$) denote the outward unit vector normal to the solid (resp. void) phase. Figure 1 schematically represents the two distinct domains as well as the immersion process of the solid domain within the void domain.

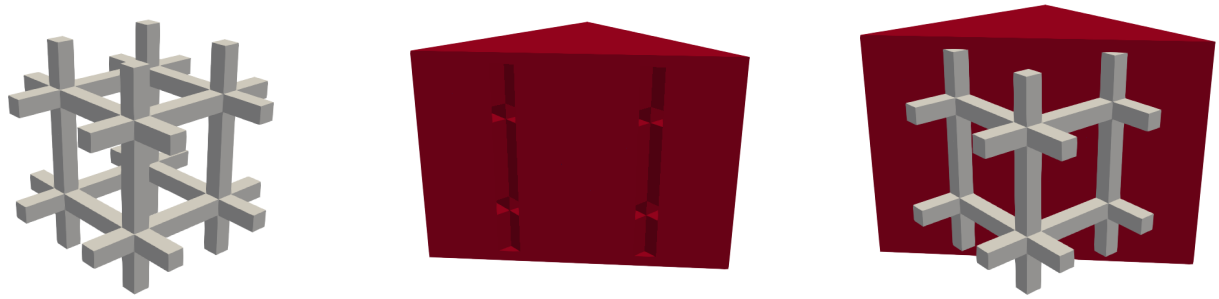

Figure 1: Computational domains used in the discrete-scale approach. Left: the solid phase Ω_s only; middle: the void phase Ω_v only; right: immersion of Ω_s into Ω_v.

The discrete-scale coupled model is quite similar to the one presented in [19]; it is however, for the sake of clarity, given hereafter.

The steady-state heat conduction equation is solved in the solid phase only. Since this phase is assumed to be opaque, the energy transfer between both phases occurs on the boundary only and, consequently, no source term is involved in this partial differential equation. The conduction problem then consists in searching for a scalar-valued function $T_\mathrm{s} :\ \Omega_\mathrm{s} \mapsto \mathbb{R}$ such that:

$$\mathcal{E}_{\mathrm{HCE}}^{\text{DS-CM}} := -\nabla \cdot \lambda_\mathrm{s} \nabla T_\mathrm{s} = 0 \quad \forall \boldsymbol{x} \in \Omega_\mathrm{s} \subset \mathbb{R}^3 \tag{1}$$

where λ_s denotes the thermal conductivity of the solid phase. Similarly to both other models presented hereafter, temperature is prescribed at the two ends of the medium, so:

$$T_\mathrm{s} = T_{g_-} \qquad \text{on } \partial\Omega_{\mathrm{s},D,-} \subset \Gamma; \partial\Omega_{\mathrm{s},D,-} = \{\boldsymbol{x} \in \partial\Omega_\mathrm{s},\ \boldsymbol{x} < \delta + \min_{\Omega_\mathrm{s}} \boldsymbol{x}'\}, \tag{2}$$

$$T_\mathrm{s} = T_{g_+} \qquad \text{on } \partial\Omega_{\mathrm{s},D,+} \subset \Gamma; \partial\Omega_{\mathrm{s},D,+} = \{\boldsymbol{x} \in \partial\Omega_\mathrm{s},\ \boldsymbol{x} < -\delta + \max_{\Omega_\mathrm{s}} \boldsymbol{x}'\}. \tag{3}$$

In these relationships, the subscript 'D' stands for 'Dirichlet', and δ is a sufficiently small positive user-defined parameter so that the Dirichlet condition is applied on a boundary of sufficiently large enough area, i.e. $|\partial\Omega_{\mathrm{s},D,\pm}| > \epsilon$. T_{g_+} and T_{g_-} are the given hot and cold Dirichlet temperatures, respectively.

The conduction equation in the solid phase is additionally supplied with the flux exchange condition which takes place on the boundary and which takes into account of both the outgoing and incoming radiation:

$$-\lambda_\mathrm{s} \nabla T_\mathrm{s} \cdot \boldsymbol{n}_\mathrm{s} = \varepsilon_\mathrm{s}\ \sigma_\mathrm{B}\ n_\mathrm{s}^2\ (T_\mathrm{s})^4 - \varepsilon_\mathrm{s} \int_{\boldsymbol{s}\cdot\boldsymbol{n}_\mathrm{v}>0} I_\mathrm{v} \boldsymbol{s} \cdot \boldsymbol{n}_\mathrm{v}\ \ \mathrm{d}\boldsymbol{s} \tag{4}$$

In this equation, T_s represents the solid-void interface temperature, ε_s denotes the emissivity of the solid medium, σ_B denotes the Stefan–Boltzmann's constant, n_s is the refraction index of the solid phase. The first term in the right-hand side of the equality sign denotes the emission loss, while the second term denotes the incoming radiation flux.

We further use the steady-state radiative transfer equations for the void which is non absorbing and non scattering medium, and where no emission occurs:

$$\mathcal{E}_{\mathrm{RTE}}^{\text{DS-CM}} := \boldsymbol{s} \cdot \nabla I_\mathrm{v} = 0 \tag{5}$$

The non-zero temperature yielding emission on the common void-solid boundary Γ comes into play as the boundary-value condition (the hat symbol stands for the 'inlet' condition), and the specular reflection boundary condition is also prescribed (it is the same type as for the continuous-scale coupled model):

$$\widehat{I}_\mathrm{v}(\boldsymbol{x}, \boldsymbol{s}) = \frac{1}{\pi} \sigma_B\ \varepsilon_\mathrm{s}\ n_\mathrm{s}^2\, (T_\mathrm{s})^4 + (1 - \epsilon_\mathrm{s}) I_\mathrm{v}(\boldsymbol{x}, \boldsymbol{s}') \quad \text{on } \Gamma, \boldsymbol{s} \cdot \boldsymbol{n}_\mathrm{v} < 0 \tag{6}$$

with $\rho_s = 1 - \varepsilon_s$ denotes the surface reflectivity. Eventually, on the two ends of the domain, hot and cold temperature are prescribed, yielding the emission condition:

$$I_v(\boldsymbol{x}, \boldsymbol{s}) = \epsilon \frac{1}{\pi} \sigma_B n^2 T_{g_\mp}^4 \quad \forall x = \{x_{\min}, x_{\max}\} \tag{7}$$

To sum-up on this configuration, a solid medium is immersed within a void region represented by the bounding box such that the solid medium does not touch any boundary of the bounding box. The radiation that goes out of these six boundaries of the bounding box reenters the bounding box due to specular reflection. On the junction between the solid and the void, there is an energy exchange: there is emission due to temperature (from solid to void), radiation absorption (from void to solid), and partial reflection of the radiation (from void to void). Additionally, on two extreme parts of the solid medium, the temperature is prescribed such that a temperature gradient is numerically created.

2.2. The continuous-scale coupled model (CS-CM)

In order to describe the mathematical model that governs the radiation physics coupled with the conduction one, in a continuous medium, let us denote the open bounded set $\Omega \subset \mathbb{R}^3$ that represents the spatial domain of interest. (In the present study, this domain is a parallelepiped, i.e. $\Omega = \{(x, y, z) | x \in [0, L_x],\ y \in [0, L_y],\ z \in [0, L_z], \}$.) The boundary of the domain, denoted as $\partial\Omega$, forms the union of Neumann and Dirichlet conditions, denoted as Γ_N and Γ_D, respectively, and Γ_D itself is the union of Γ_D^+ and Γ_D^-, such that different conditions can be applied on the boundary of the three-dimensional domain, such as prescribed temperature, adiabatic condition, reflection of radiative intensity, emission, etc. For the mathematical derivations, let $\boldsymbol{n}$ denote the outward unit vector normal to domain Ω.

In this work, we use the standard steady-state form of the radiative transfer equation which allows to describe the propagation of thermal radiation through a medium affected by absorption, emission and scattering processes. The mathematical statements, based on the principle of energy conservation, leading to this integro-differential equation are given for example in [21, 22]. Its use requires to carefully check that the textural features of the porous medium allow to fulfill the assumptions of *randomness*, *homogeneity*, and *continuity* [23]. The condition of randomness is fulfilled because, as seen in next sections, the geometric clearance is higher than the radiative wavelengths, and the condition of homogeneity is fulfilled because the typical size of individual scatterers is smaller than the characteristic size of the medium. Eventually, homogeneity is essential for considering the porous medium as a continuous one. Also, though the generalized radiative transfer equation [24] is to be applied in low porosity media, the ordinary version of the radiative transfer equation is considered as valid in the high porosity media considered here:

$$\mathcal{E}_{\text{RTE}}^{\text{CS-CM}} := \boldsymbol{s} \cdot \nabla I(\boldsymbol{x}, \boldsymbol{s}) + \beta I(\boldsymbol{x}, \boldsymbol{s}) - \sigma \int_{4\pi} I(\boldsymbol{x}, \boldsymbol{s}') \Phi(\boldsymbol{s}, \boldsymbol{s}')\ \mathrm{d}\boldsymbol{s}' - \kappa \frac{1}{\pi} \sigma_B n^2 T^4 = 0 \tag{8}$$

In this equation, $\boldsymbol{x} = (x, y, z) \in \Omega$, $\boldsymbol{s} \in \mathcal{S}^2$ is the direction of propagation, $\beta = \kappa + \sigma$ is the extinction coefficient, σ is the scattering coefficient, κ is the absorbtion coefficient, σ_B is the Stephan-Boltzmann constant, n is the refraction index of the medium, and T is the temperature. Also, $\Phi(\boldsymbol{s}, \boldsymbol{s}')$ is the phase function which can be determined by numerical means. For example, based on a statistical representation of the porous medium, the radiative distribution function identification (RDFI) method completely characterizes this scattering phase function [25, 26]. In the present study, among other possible approximations, the Henyey-Greenstein function is used. For three-dimensional domains, the normalised Henyey-Greenstein function reads:

$$\Phi(\boldsymbol{s}, \boldsymbol{s}') = \frac{1}{4\pi} \frac{1 - g^2}{(1 + g^2 - 2g\boldsymbol{s} \cdot \boldsymbol{s}')^{\frac{3}{2}}} \tag{9}$$

where $g \in]-1, 1[$ is the anisotropy factor. The integro-differential eq. (8) for the transport of radiation comes with its boundary conditions. In order to mimic emission where temperature is prescribed, i.e. on $x = x_{\min}$ and $x = x_{\max}$, and periodicity on other boundaries (with specular reflection), one lets, for $\boldsymbol{s} \cdot \boldsymbol{n} < 0$:

$$I(\boldsymbol{x}, \boldsymbol{s}) = \epsilon \frac{1}{\pi} \sigma_B n^2 T^4 \qquad \forall x = \{x_{\min}, x_{\max}\} \tag{10}$$

$$I(\boldsymbol{x}, \boldsymbol{s}) = (1 - \epsilon) I(\boldsymbol{x}, \boldsymbol{s}') \quad \forall x \in]x_{\min}, x_{\max}[\tag{11}$$

where ϵ the emissivity of the boundary, and $\boldsymbol{s}'$ is deduced from $\boldsymbol{s}$ from the Householder rotation matrix $\mathcal{R}(\boldsymbol{n}) = 2\boldsymbol{n}\boldsymbol{n}^\top - I$, following [27].

The steady-state heat conduction equation involving the radiation contribution consists in equaling both fluxes of conduction and radiation. The former is given by the Fourier law, and the latter is the radiative source term. One gets [21]:

$$\mathcal{E}_{\text{HCE}}^{\text{CS-CM}} := \nabla \cdot (-\lambda \nabla T) + k 4\pi I_b - kG = 0 \tag{12}$$

with λ being the thermal conductivity. In this equilibrium equation, G denotes the radiative density and I_b denotes black body source term:

$$G(x) = \int_{4\pi} I(x, S)\ \mathrm{d}\boldsymbol{s} \tag{13}$$

$$I_b = I_b(T) := \frac{1}{\pi}\sigma_B n^2 T^4 \tag{14}$$

The partial differential eq. (12) for the heat conduction comes with its boundary conditions. Temperature is prescribed on $x = x_{\min}$ and $x = x_{\max}$, and adiabatic condition is prescribed everywhere else:

$$T = T^- \qquad \forall x = \{x_{\min}\} \tag{15}$$

$$T = T^+ \qquad \forall x = \{x_{\max}\} \tag{16}$$

$$-\nabla T \cdot \boldsymbol{n} = T_N = 0 \quad x \in]x_{\min}, x_{\max}[\tag{17}$$

2.3. The continuous-scale Rosseland model (CS-RM)

In the Rosseland approximation, the radiative source term is an explicit non-linear function of the temperature, according to, for instance, [21]:

$$\mathcal{E}^{\text{CS-RM}} := -\nabla \cdot (\lambda \nabla T) - \nabla \cdot (\alpha T^3 \nabla T) = 0 \tag{18}$$

with

$$\alpha = \frac{16 n^2 \sigma_B}{3\beta} \tag{19}$$

where n is the refraction index, σ_B the Stephan-Boltzmann constant, and β the extinction coefficient. Note that the Rosseland approximation is usually to be used only on optically thick media; the criterion $\beta L > 5$ is, for instance given in [28], with $L = |x_{\max} - x_{\min}|$ the length towards the main direction of propagation. Added to this non-linear partial differential equation, the boundary conditions (15)-(17) are to be applied.

3. Resolution in a finite element framework

Three distinct physical models have been presented in section 2 in order to solve the conducto-radiative coupled physics in a bounded domain, in both continuous and discrete scales.

The radiative transfer equation involving absorption, scattering and emission is involved in the continuous-scale coupled model (CS-CM), see eq. (8), while it is mathematically simplified to a transport advection-type equation in the discrete-scale coupled model (DS-CM), see eq. (5). In the following, the solution process is given only for the full RTE, i.e. for $\mathcal{E}_{\text{RTE}}^{\text{CS-CM}}$; the process being easily transposed to the discrete-scale, i.e. for $\mathcal{E}_{\text{RTE}}^{\text{DS-CM}}$. The solution of the RTE with vectorial finite elements is the subject of section 3.1; additional details can be found in [13] and accompanying papers.

Besides the radiative equation, a non-linear heat conduction equation is also to be solved. Due to its non-linear character, the equation has to be linearized, and an iterative scheme is set-up to make the state converge to the right solution.

Section 3.1 deals with the finite element set-up and the variational formulation for solving the radiative transfer equation; section 3.2 deals with the variational formulation and iterative schemes for solving the non-linear heat conduction equation; section 3.3 deals with the variational formulation and iterative schemes for solving the non-linear Rosseland approximation model; eventually, section 3.4 gives the global iterative process.

3.1. Vectorial finite elements and discrete ordinates for solving the radiative transfer equation

The discrete ordinate method is used to angularly semi-discretize the RTE. Choosing, in an appropriate way, N_d couples of direction/weight, using, for example, the S_N method, or any other method based on the discretization of the unit sphere (in the current study we use the uniformly refined octahedron, as presented in [18]), the problem consists in solving, $\forall m = 1, \ldots, N_d$:

$$(\boldsymbol{s}_m \cdot \nabla + \beta) I_m(\boldsymbol{x}) = \sigma \sum_{n=1}^{N_d} \omega_m I_n \Phi_{m,n} + \kappa I_b \tag{20}$$

The vectorial finite element method consists in searching a vector of radiative intensities $\mathbb{I}$ (vectorial trial function) using a vectorial test function $\mathbb{W}$ which lies in the corresponding vectorial functional space $\mathbf{V} := \Pi_{i=1}^{N_d} \mathcal{V}_i$. In order to derive the vectorial FEM variational formulations for equation (20), the first step is to convert coupled set of equations (20) into its equivalent vectorial form. To do that, let us first define the

radiative intensities vector $\mathbb{I}$, the collective direction vector $\mathbb{S}$ collecting all individual directions vectors S_m, and a matrix Θ of size $N_d \times N_d$ that combines scattering coefficient σ_s, weights ω_m, and scattering phase function $\Phi_{m,n}$. These quantities are expressed as:

$$\mathbb{I} = \begin{pmatrix} I_1 \\ I_2 \\ \vdots \\ I_{N_d} \end{pmatrix}, \quad \mathbb{S} = \begin{pmatrix} \boldsymbol{s}_1 \\ \boldsymbol{s}_2 \\ \vdots \\ \boldsymbol{s}_{N_d} \end{pmatrix}, \quad \Theta = \begin{pmatrix} \sigma_s\omega_1\phi_{1,1} & \sigma_s\omega_2\phi_{1,2} & \dots & \sigma_s\omega_{N_d}\phi_{1,N_d} \\ \sigma_s\omega_1\phi_{2,1} & \sigma_s\omega_2\phi_{2,2} & \dots & \sigma_s\omega_{N_d}\phi_{2,N_d} \\ \vdots & \ddots & \vdots & \vdots \\ \sigma_s\omega_1\phi_{N_d,1} & \sigma_s\omega_2\phi_{N_d,2} & \dots & \sigma_s\omega_{N_d}\phi_{N_d,N_d} \end{pmatrix} \tag{21}$$

Using these notations, the RTE in its discrete ordinates form, eq. (20), can now be reformulated in its equivalent vectorial form. The vectorial equation reads:

$$\mathbb{S} \cdot \nabla\mathbb{I} + \beta\mathbb{I} - \Theta\mathbb{I} = \kappa I_b \mathbb{I}_d \tag{22}$$

with $\mathbb{I}_d$ being the identity vector of same order as $\mathbb{I}$. Here, $\mathbb{S} \cdot \mathbb{I}$ would give a vector, the ith component of which will be given by $(\mathbb{S} \cdot \mathbb{I})_i = s_i \cdot \nabla I_i$. Let us also introduce the following notations: $\mathbb{A}^T\mathbb{B} = \sum_i \mathbb{A}_i\mathbb{B}_i$ and $(\mathbb{A} : \mathbb{B}) = \mathbb{A}_i\mathbb{B}_i$. The vectorial FEM weak formulation can now be built by multiplying the vectorial eq. (22) with the SUPG vectorial test function $\mathbb{W} + \gamma\mathbb{S} \cdot \nabla\mathbb{W}$ and integrating over the domain of interest Ω. Based on that, the problem now reads: search $\mathbb{I}$ in $\mathbf{V}$ that satisfies:

$$\int_\Omega (\mathbb{S} \cdot \nabla\mathbb{I} + \beta\mathbb{I})^T(\mathbb{W} + \gamma\mathbb{S} \cdot \nabla\mathbb{W}) \, \mathrm{d}\boldsymbol{x} - \int_\Omega (\Theta\mathbb{I})^T(\mathbb{W} + \gamma\mathbb{S} \cdot \nabla\mathbb{W}) \, \mathrm{d}\boldsymbol{x} = \int_\Omega (kI_{b,T}\mathbb{I}_d)^T(\mathbb{W} + \gamma\mathbb{S} \cdot \nabla\mathbb{W}) \, \mathrm{d}\boldsymbol{x} \quad \forall\mathbb{W} \in \mathbf{V} \tag{23}$$

The Green theorem is then applied for introducing the inflow boundary conditions, so that the problem consists in searching $\mathbb{I}$ in $\mathbf{V}^h$ that satisfies:

$$\begin{aligned} \int_\Omega (\mathbb{S} \cdot \nabla\mathbb{W})^T\mathbb{I} \, \mathrm{d}\boldsymbol{x} + \int_{\partial\Omega} (\mathbb{S} \cdot \mathbf{n}) : \mathbb{H}_{[\mathbb{S}\cdot\mathbf{n}>0]})^T\mathbb{W} \, \mathrm{d}\boldsymbol{x} \\ + \int_{\partial\Omega} (\mathbb{S} \cdot \mathbf{n} : \mathbb{H}_{[\mathbb{S}\cdot\mathbf{n}<0]} : \mathbb{I}_{in})^T\mathbb{W} \, \mathrm{d}\boldsymbol{x} \int_\Omega (\mathbb{S} \cdot \nabla\mathbb{I})^T(\gamma\mathbb{S} \cdot \nabla\mathbb{W}) \, \mathrm{d}\boldsymbol{x} \\ + \int_\Omega (\beta\mathbb{I})^T(\mathbb{W} + \gamma\mathbb{S} \cdot \nabla\mathbb{W}) \, \mathrm{d}\boldsymbol{x} - \int_\Omega (\Theta\mathbb{I})^T(\mathbb{W} + \gamma\mathbb{S} \cdot \nabla\mathbb{W}) \, \mathrm{d}\boldsymbol{x} \\ = \int_\Omega (kI_b\mathbb{I}_d)^T(\mathbb{W} + \gamma\mathbb{S} \cdot \nabla\mathbb{W}) \, \mathrm{d}\boldsymbol{x} \qquad \mathbb{W} \in \mathbf{V} \end{aligned} \tag{24}$$

where $\mathbb{H}_{[\mathbb{S}\cdot\mathbf{n}>0]}$ is the vectorial indicator (Heaviside) function. This function results in zeros and ones depending on Boolean operations, e.g., $\mathbb{H}_{[\mathbb{S}\cdot\mathbf{n}>0]_i}$ equals one if and only if si $\mathbb{S} \cdot \mathbf{n} > 0$, and zero elsewhere.

In typical treated situations, hundreds of directions are needed in the discrete ordinate method, and a fine enough spatial discretization is also needed to ensure that the numerical solution is close enough to the real solution. This yields huge matrix systems after approximating (24). To cope with such difficulties, domain decomposition approach is performed on this vectorial equation, see [14], the use of efficient solvers based on Krylov-subspace methods are used, see [16], and semi-matrix free approach is set-up on the top of (24), see [15]. Note that this solver handles both absorbing-scattering and non absorbing-non scattering media in the same way; just physical properties are set to zero for the latter kind of medium.

3.2. Newton–Raphson and finite elements for solving the heat conduction equation

In order to give the finite element discretization of $\mathcal{L}_{\mathrm{HCE}}^{\mathrm{CS\text{-}CM}}$, we introduce the following Sobolev spaces [29]:

$$H_0 := \{\phi \in L^2(\Omega) \quad / \quad \nabla\phi \in (L^2(\Omega))^d\}, \tag{25}$$

$$H_{\Gamma^-} := \{\phi \in H^1(\Omega), \quad \phi = 0 \quad \text{on } \Gamma_D^-\}, \tag{26}$$

$$H_{\Gamma^+} := \{\phi \in H^1(\Omega), \quad \phi = 0 \quad \text{on } \Gamma_D^+\}. \tag{27}$$

To begin with, the partial differential equation eq. (12) is multiplied by a test function belonging to the above functional space and integrated over the whole domain of integration Ω. Then, in order to introduce the Neumman boundary conditions, we apply Green's formula on the first integrand so that, eventually, the weak formulation yields in finding $T \in (T^- + H_{\Gamma^-}) \cap (T^+ + H_{\Gamma^+})$, such that

$$\int_\Omega \lambda\nabla T \cdot \nabla v \, \mathrm{d}\boldsymbol{x} = \int_\Omega \kappa\tilde{G}v \, \mathrm{d}\boldsymbol{x} - \int_\Omega (\kappa 4\sigma_B n^2 T^4)v \, \mathrm{d}\boldsymbol{x} \qquad \forall v \in H_0. \tag{28}$$

Equation (28) is nonlinear. Therefore, starting from an initial guess condition, say T_0, an iterative scheme is to be set-up coupled with a linearization of the equation. Three linearization methods are presented hereafter (these methods shall be compared in the numerical results dedicated section).

1. The ordinary fixed-point method consists in expressing the non-linear term with the state given at the previous iteration. Denoting $k+1$ the current iteration, and k the previous iteration, this yields in searching $T_{k+1} \in (T^- + H_{\Gamma^-}) \cap (T^+ + H_{\Gamma^+})$, $k \in \mathbb{N}^+$, that satisfies:

$$\int_\Omega \lambda \nabla T_{k+1} \cdot \nabla v \, \mathrm{d}\boldsymbol{x} = \int_\Omega \kappa \tilde{G} \, \mathrm{d}\boldsymbol{x} - \int_\Omega \kappa 4 \sigma_B n^2 T_k^4) v \, \mathrm{d}\boldsymbol{x} \quad \forall v \in H_0 \tag{29}$$

2. The improved fixed-point method consists in linearizing the non-linear term such that, at the current iteration, one writes $T^4 = T_{k+1} T_k^3$. This strategy yields in searching $T_{k+1} \in (T^- + H_{\Gamma^-}) \cap (T^+ + H_{\Gamma^+})$ such that:

$$\int_\Omega \lambda \nabla T_{k+1} \cdot \nabla v \, \mathrm{d}\boldsymbol{x} + \int_\Omega \kappa 4 \sigma_B n^2 T_k^3 T_{k+1} v \, \mathrm{d}\boldsymbol{x} = \int_\Omega \kappa \tilde{G} v \, \mathrm{d}\boldsymbol{x} \quad \forall v \in H_0. \tag{30}$$

3. the Newton–Raphson linearization method [30] directly applied on the weak formulation eq. (28) is here proposed as a third method. After some mathematical manipulations, the finite element discretization of the non-linear heat conduction problem, using the Newton–Raphson linearization method, consists in searching $T_{k+1} \in (T^- + H_{\Gamma^-}) \cap (T^+ + H_{\Gamma^+})$ such that:

$$\int_\Omega \lambda \nabla T_{k+1} \cdot \nabla v \, \mathrm{d}\boldsymbol{x} + \int_\Omega 4\kappa 4\pi \frac{1}{\pi} \sigma_B n^2 T_k^3 T_{k+1} v \, \mathrm{d}\boldsymbol{x} = \int_\Omega 3(\kappa 4 \sigma_B n^2 T_k^4) v \, \mathrm{d}\boldsymbol{x} + \int_\Omega (\kappa \tilde{G}) v \, \mathrm{d}\boldsymbol{x} \qquad \forall v \in H_0. \tag{31}$$

3.3. Newton–Raphson and finite elements for solving the Rosseland approximation

The Rosseland approximation eq. (18) which couples both physics of conduction and radiation yields a nonlinear equation. To solve this equation, finite elements are used along with an iterative scheme based on a linearization of the equation. The same functional space as the one used in section 3.2 is introduced, so that the variational formulation reads:

$$\int_\Omega \lambda \nabla T \cdot \nabla \varphi \, \mathrm{d}\boldsymbol{x} + \int_\Omega \alpha T^3 \nabla T \cdot \nabla \varphi \, \mathrm{d}\boldsymbol{x} = 0 \qquad \forall \varphi \in H_0. \tag{32}$$

Equation (28) is nonlinear. Therefore, starting from an initial guess condition, say T_0, an iterative scheme is to be set-up coupled with a linearization of the equation. Two linearization methods are presented hereafter (these methods shall be compared in the numerical results dedicated section).

1. The ordinary fixed-point method consists in expressing the non-linear term with the state given at the previous iteration. Denoting $k+1$ the current iteration, and k the previous iteration, this yields in searching $T_{k+1} \in (T^- + H_{\Gamma^-}) \cap (T^+ + H_{\Gamma^+})$, $k \in \mathbb{N}^+$, that satisfies:

$$\int_\Omega \lambda \nabla T_{k+1} \cdot \nabla \varphi \, \mathrm{d}\boldsymbol{x} + \int_\Omega \alpha T_k^3 \nabla T_{k+1} \cdot \nabla \varphi \, \mathrm{d}\boldsymbol{x} = 0 \qquad \forall \varphi \in H_0. \tag{33}$$

   where H_0, H_{Γ^+} and H_{Γ^-} are respectively the Sobolev spaces given in previous section, φ is the test function and T_0 is initial guess condition.

2. the Newton–Raphson linearization method [30] directly applied on the weak formulation eq. (32) is here proposed as a second method. After some mathematical manipulations, the finite element discretization of the non-linear heat conduction problem, using the Newton–Raphson linearization method, consists in searching $T_{k+1} \in (T^- + H_{\Gamma^-}) \cap (T^+ + H_{\Gamma^+})$ such that:

$$\int_\Omega \lambda \nabla T_{k+1} \cdot \nabla \varphi \, \mathrm{d}\boldsymbol{x} + \int_\Omega 3\alpha T_k^2 T_{k+1} \nabla T_k \cdot \nabla \varphi \, \mathrm{d}\boldsymbol{x} + \int_\Omega \alpha T_k^3 \nabla T_{k+1} \cdot \nabla \varphi \, \mathrm{d}\boldsymbol{x} = \int_\Omega 3\alpha T_k^3 \nabla T_k \cdot \nabla \varphi \, \mathrm{d}\boldsymbol{x} \quad \forall \varphi \in H_0 \tag{34}$$

3.4. Numerical algorithm for solving the coupled problem

Added to non-linear conduction equations, the coupling itself between both radiation and conduction physics makes the problem to be non-linear. It is suggested the two physics are solved iteratively, one after the other. The following algorithm 1 has been set-up for the continuous-scale coupled model.

A linear steady-state heat conduction equation is firstly solved in order to get the initial guess (see line 5), which is needed to start the iterations. The outer loop (see line 7) is used to solve successively the radiative and then the conduction equation until stabilization is reached. The stabilization criterion is based on the infinite-based norm (in space) on temperature difference between the current iteration and the previous one, within the outer loop, but out of the next inner loop. The inner loop (see 12) is used for the non-linear heat conduction equation, until a stabilization criterion is satisfied; this one is based on the spatial infinite-based norm of the difference between the current iteration and the previous one, within the inner loop.

The set-up for the DS-CM can be easily derived from this one.

Algorithm 1 Iterative algorithm for solving the continuous-scale coupled conducto-radiative problem.

input parameters for the geometry; physical properties
load spatial and angular discretizations
define finite element spaces
$k \leftarrow 0$
solve $-\lambda \Delta \bar{T} = 0$ **return** $\bar{T}$
$T_{in} \leftarrow \bar{T}$
for $k \leftarrow 1$ **to** k_{max} **do**
    $l \leftarrow 0$
    $T^{(k,l)} \leftarrow T_{in}$
    calculate $I_b = I_b(T^{(k,l)})$
    solve RTE **return** $\mathbb{I}^h$
    for $l \leftarrow 1$ **to** l_{max} **do**
        solve Conduction using $\mathbb{I}^h$ **return** $T^{(k,l)}$
        $e^{(l)} \leftarrow \|T^{(k,l)} - T^{(k,l-1)}\|_\infty$
        if $e^{(l)} < \varepsilon_l$ **then**
            break
        end if
        $T^{(k,l-1)} \leftarrow T^{(k,l)}$
    end for
    $\hat{l}(k) \leftarrow l$
    $T^k \leftarrow T^{(k,\hat{l})}$
    $E^{(k)} \leftarrow \|T^{(k)} - T^{(k-1)}\|_\infty$
    if $E^{(k)} < \varepsilon_k$ **then**
        break
    end if
    $T_{in} \leftarrow T^{(k)}$
end for

4. Set-up numerical validations and comparisons

This preliminary section details the set-up of all necessary tools used for validations, convergence analysis, and comparisons between models, all these being given in the next section.

4.1. Non-dimensional numbers

Hereafter are given the necessary non-dimensional numbers used in the next section, for characterizing tests, plot figures, and do proper comparisons:

- A dimensionless temperature $\Theta(\boldsymbol{x})$ as well as the reference dimensionless temperature Θ_0 are defined using temperature of both the hot and the cold plates:

$$\Theta(\boldsymbol{x}) = \frac{T(\boldsymbol{x})}{T_{max}}; \quad \Theta_0 = \frac{T_{\min}}{T_{\max}} \tag{35}$$

- The optical thickness parameter $\tau(x)$ and the optical thickness of the medium, τ_0, are defined by, respectively:

$$\tau(x) = \int_0^x \beta \, \mathrm{d}x = \beta x; \quad \tau_0 = \beta L \tag{36}$$

  In the next section, most plots will consider dimensionless temperature Θ as a function of the optical thickness $\tau(x)$.

- The albedo of single scattering, also known as the Schuster number [31], is defined as the ratio between the scattering coefficient and the absorption coefficient. Both these relationships will be used in th next section:

$$\omega = \frac{\sigma}{\beta}; \quad \frac{\kappa}{\beta} = 1 - \omega \tag{37}$$

  Note that, at continuous scale, the albedo of single scattering is related to the emissivity, through:

$$\omega = 1 - \varepsilon \tag{38}$$

- The conduction-to-radiation parameter [21, 31], also known as the Plank number, or the Stark number, determines the relative role of both the conduction and radiative physics: conduction predominates for large N, while radiation predominates for low N.

$$\mathrm{N} = \frac{\lambda\beta}{4\sigma_B T_{\max}^3} \tag{39}$$

4.2. Geometry definition

The three-dimensional geometry used for continuous-scale models is a rectangular parallelepiped (note that this geometry has been prefered to the ordinary cube in order to save computational resources):

$$\Omega = \left]-\frac{L}{2},\frac{L}{2}\right[\times \left]-\frac{L}{6},\frac{L}{6}\right[\times \left]-\frac{L}{6},\frac{L}{6}\right[\tag{40}$$

The chosen related discrete-scale geometry is the one defined by Perrausin and Haussener [20], and shown schematically in fig. 2-left. It is composed of squared-section bars. Symbols L, ℓ, and d_{nom} denote the full length (it is the one used in the continuous-scale geometry), the squared-section size, and the nominal diameter of the pore, respectively. This geometry in fact is a single cell of a much bigger open-cell foam which is composed of these unit cells, see fig. 2-right. From geometrical considerations, both the porosity and the pore nominal diameter can be expressed explicitly as a function of the pore nominal diameter:

$$p(\ell) = \frac{L^3 - 12\ell^2 L + 16\ell^3}{L^3}; \quad d(\ell) = \frac{L - 2\ell}{2} \tag{41}$$

Besides, following [32, 33], the effective extinction coefficient relative to a discrete-scale media is an explicit function of both the porosity and the pore nominal diameter, see eq. (45). So, for the given geometry composed of squared bars as presented in fig. 2, for a given full length L, and for a given effective extinction coefficient β, the bar width ℓ is to be solution of:

$$\ell^3 - \frac{288L}{384}\ell^2 - \frac{5\beta L^3}{384}\ell + \frac{5\beta L^4}{768} = 0 \tag{42}$$

This third-degree equation has three solutions. With the given values of L and β, the unique positive real solution is given by [34]:

$$\ell = 2\sqrt{-Q}\cos\left(\frac{1}{3}\varphi\right) - \frac{1}{3}a_1 \tag{43}$$

with

$$a_1 = \frac{-288L}{384}; \qquad a_2 = \tfrac{-5\beta L^3}{384}; \qquad a_3 = \frac{5\beta L^4}{768};$$
$$Q = \frac{3a_2 - a_1^2}{9} \quad R = \tfrac{9a_1a_2 - 27a_3 - 2a_1^3}{54}; \quad \varphi = \arccos R/\sqrt{-Q^3}$$

As reported in table 2, for exemple for $L = 3.8 \times 10^{-4}$ m, and $\beta = 2624.67$, the porosity p has been found to be approximately equal to 0.9127, the nominal diameter of the pore $d_{\mathrm{nom}} \approx 1.5963 \times 10^{-4}$ m, and the squared section width $\ell \approx 3.0869 \times 10^{-5}$ m.

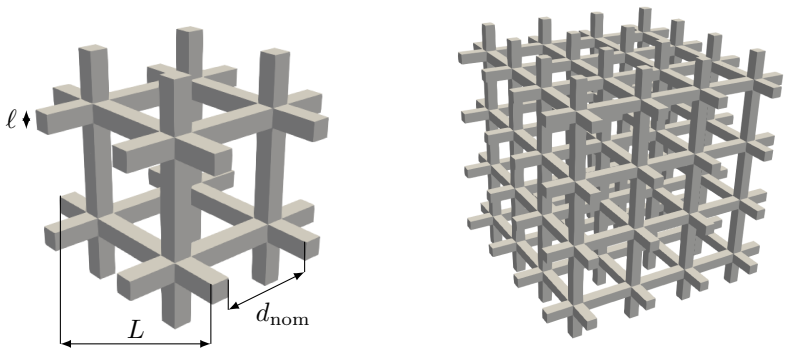

Figure 2: Schematic representation of the discrete-scale geometry composed of crossed bars.

4.3. Set-up physical properties from discrete to continuous scale and vice-versa

Effective physical properties of a porous medium are functions of properties of the different phases at the discrete scale as well as on geometric characteristics. The determination of such effective properties by upscaling-type approaches is an active research subject as been denoted very recently [35]. In the radiative transfer community, usual routes are based on numerical tools such as Monte-Carlo or ray tracing simulations on representative elementary volumes [36, 37]. Following for example [32, 33, 38], the effective conductivity λ, the effective extinction coefficient β, and the effective emissivity ε are given by:

$$\lambda = \frac{1}{3}(1-p)\lambda_{\rm s} \tag{44}$$

$$\beta = 4.8\frac{1-p}{d_{\rm nom}} \tag{45}$$

$$\varepsilon = 1-(1-\varepsilon_{\rm s})\times(1-0.8p) \tag{46}$$

where $\lambda_{\rm s}$, and $\varepsilon_{\rm s}$ are the thermal conductivity, the emissivity of the solid phase involved in the discrete-scale model, and p and $d_{\rm nom}$ denote the porosity and the nominal diameter of the pore, respectively. Note that the single scattering albedo and the emissivity in the continuous-scale case are denoted by ω and ε, respectively, while, however, in the discrete-scale case, they are denoted by ω_s and ε_s, respectively.

In order to perform the passage from the discrete scale to the continuous scale, and vice-versa, let us first point out that the continuous-scale coupled model is fully defined by these four parameters: *i*) the effective thermal conductivity λ, *ii*) the effective absorption coefficient κ, *iii*) the effective scattering coefficient σ, and *iv*) the effective emissivity of the medium ϵ. Besides, the discrete-scale coupled model is fully defined by these four parameters: *i*) the solid-phase thermal conductivity $\lambda_{\rm s}$, *ii*) the solid-phase emissivity ε, *iii*) the porosity p, and *iv*) the nominal diameter of the pore $d_{\rm nom}$.

- The knowledge of effective properties at the continuous scale, for a given geometry (so for a given porosity and nominal pore diameter) gives directly, using eqs. (44) and (46), both the thermal conductivity and the emissivity of the solid phase:

$$\lambda_{\rm s} = 3\frac{\lambda}{1-p} \tag{47}$$

$$\varepsilon_{\rm s} = 1-\frac{1-\varepsilon}{1-\frac{4}{5}p} \tag{48}$$

- At the discrete scale, the knowledge of the solid-phase properties $\lambda_{\rm s}$ and $\varepsilon_{\rm s}$ along with the porosity p and the pore nominal diameter $d_{\rm nom}$, determines the continuous-scale model, as follows. Firstly, eqs. (44) and (46) give directly the effective thermal conductivity λ and the effective emissivity ε. Then, combining eqs. (37) to (39) and (44) to (46) yields the Stark number N as an explicit function of λ, p, and $d_{\rm nom}$, see eq. (49). The effective absorption coefficient κ is then expressed as an explicit function of the Stark number N, the solid-phase emissivity $\varepsilon_{\rm s}$, the porosity p, and the effective thermal conductivity λ, see eq. (50). Eventually, the effective scattering coefficient σ is expressed as an explicit function of solid-phase emissivity $\varepsilon_{\rm s}$, the porosity p, and the effective absorption coefficient κ, see eq. (51).

$$\mathrm{N} = \frac{4.8\lambda(1-p)}{4\sigma_B T_{max}^3 d_{\rm nom}} \tag{49}$$

$$\kappa = \frac{4\sigma_B T_{max}^3 N\left(1-(1-\varepsilon_{\rm s})(1-\frac{4}{5}p)\right)}{\lambda} \tag{50}$$

$$\sigma = \left(\frac{1}{1-(1-\varepsilon_{\rm s})(1-\frac{4}{5}p)}-1\right)k \tag{51}$$

Note that the anisotropy coefficient involved in the Henyey-Greenstein approximation function eq. (9) cannot be determined directly by this upscaling-type methodology. It could however be determined by the radiative distribution function identification (RDFI) method, for example, which completely characterizes, among other quantities, the scattering phase function [25, 26]. In the current study, the anisotropy coefficient has been set to zero yielding isotropic scattering. This can be justified numerically, see section 5.1.3, because, in the configuration dealt with in this study, output temperature is little sensitive to this parameter.

4.4. Some more quantities

Some useful quantities are now defined; these are used in order to plot one-dimensional non-dimensional averaged temperature out of results obtained in three-dimensional domains, as well as to quantify errors. The

non-dimensional x-averaged temperature $\widehat{T}(x)$ is the non-dimensional averaged temperature on a given yz-plane located at a specific $x = \hat{x}$ (this plane is denoted as $\mathcal{A}_{\hat{x}}$). For the discrete scale (for the continuous-scale problems, the indicator function is taken equal to one everywhere), it is:

$$\widehat{T}(x) := \frac{1}{T_{\max}} \frac{\int_{\mathcal{A}_{\hat{x}}} T(\boldsymbol{x}) \mathbb{1}_{[\boldsymbol{x} \in \Omega_{\mathrm{s}}]} \, \mathrm{d}y \, \mathrm{d}z}{\int_{\mathcal{A}_{\hat{x}}} \mathbb{1}_{[\boldsymbol{x} \in \Omega_{\mathrm{s}}]} \, \mathrm{d}y \, \mathrm{d}z}. \tag{52}$$

Further, in order to compare the three distinct models to each other, we denote by $\widehat{e}^{\alpha-\beta}$ the difference between the computational results obtained from models α and β:

$$\widehat{e}^{\alpha-\beta}(x) = \widehat{T}^{\alpha}(x) - \widehat{T}^{\beta}(x). \tag{53}$$

and these two ordinary norms are used (the first is an averaged quadratic error norm while the second gives the maximum error along the main axis of propagation of the heat flux):

$$\widehat{e}_2(u) = \frac{1}{L} \int_0^L u^2(x) \, \mathrm{d}x; \quad \widehat{e}_\infty(u) = \max_{x \in [0,L]} |u(x)| \tag{54}$$

5. Numerical results

This section details and discusses the numerical results of the three presented models. Section 5.1 firstly presents the numerical results related to the continuous-scale coupled model, with validation and convergence analysis. Section 5.2 then presents the numerical results related to the Rosseland model, with a comparison respectively to the CS-CM, and a convergence analysis. Section 5.2 finally presents the numerical results related to the DS-CM model, with a comparison respectively to the CS-CM, and a convergence analysis.

5.1. Continuous-scale coupled model (CS-CM)

5.1.1. Validation

The validation of the three-dimensional continuous-scale coupled model is performed against the one-dimensional pioneering work of Viskanta et al. [31, 39]. Based on these references, the characteristic length L is chosen to be 3.8×10^{-4} m. The mesh needed for the approximation of the functional space is chosen to be sufficiently fine enough, and quasi-uniform, with mean size $h = L/80$. Such a choice yields $N_e = 281,247$ tetrahedral elements and $N_v = 47,068$ vertices. Further, in order to have sufficiently fine enough angular discretization, the octahedron has been refined twice, so that $N_d = 128$ directions are considered.

Following [31], the first validation is performed on an absorbing non scattering medium. Let us point out that our model is three-dimensional. Further, it involves emission on both hot and cold boundaries, it involves body emission, and it involves specular reflection on other boundaries. Specular reflections, in the present case, follow the 1-DP method, see [17]. As such, this first validation step implicitly validates all the cited mathematical operators. Following rigorously [31], the dimensionless temperature Θ_0 is set to 0.5, with $T_{\min} = 1,111$ K and $T_{\max} = 2,222$ K, the optical thickness of the medium τ_0 is set to 1 by setting the absorption coefficient κ to 2624.67 cm^{-1}.

The results are plots of adimensionalized (averaged) temperature along the main direction of propagation, x, for Stark numbers equal to 10, 1, 0.1, and 0.01 (the Stark number is modified with the value of the thermal conductivity parameter, following eq. (39)). Figure 3 presents such plots for both our results, and those from Viskanta et al. [31] (fig. 2, page 68). This figure shows that the line plots (which represent our three-dimensional results) coincide with the empty marks which represent the results obtained by Viskanta et al. in 1D. Notice however that the non-dimensional temperature for the three-diensional case is an averaged one, performed over the transverse section of the main direction of propagation of the flux, i.e. e_x, see eq. (52).

We notice that in the case of N=10 the temperature behavior is almost linear; this is explained by the fact that the conduction physics is dominant over the radiation physics. While the Stark number decreases, the radiation physics is no more negligible and, consequently, the obtained temperature profile moves away from the linear curve, see for example orange and red curves in fig. 3, for $N = 0.1$ and $N = 0.01$, respectively.

The properties needed to run this first test case are summarized in table 2 (Test A). Next, fig. 4 presents the three-dimensional temperature fields for both extreme cases, for $N = 10$, i.e. when the conduction physics predominates, and for $N = 0.01$, i.e. when radiation predominates, respectively. It can be seen from this figure how temperature is somehow homogenized due to radiation, as compared to the case where there is conduction only.

Following [39], the second validation test case considers also the scattering operator, added to all others already considered in the previous validation test case. Our numerical results are plotted and compared against those cited, setting the Stark parameter N to the value 0.1, the extinction coefficient $\beta = 2624.67$ m^{-1}, and the optical thickness to the value $\tau_0 = 1$ m.

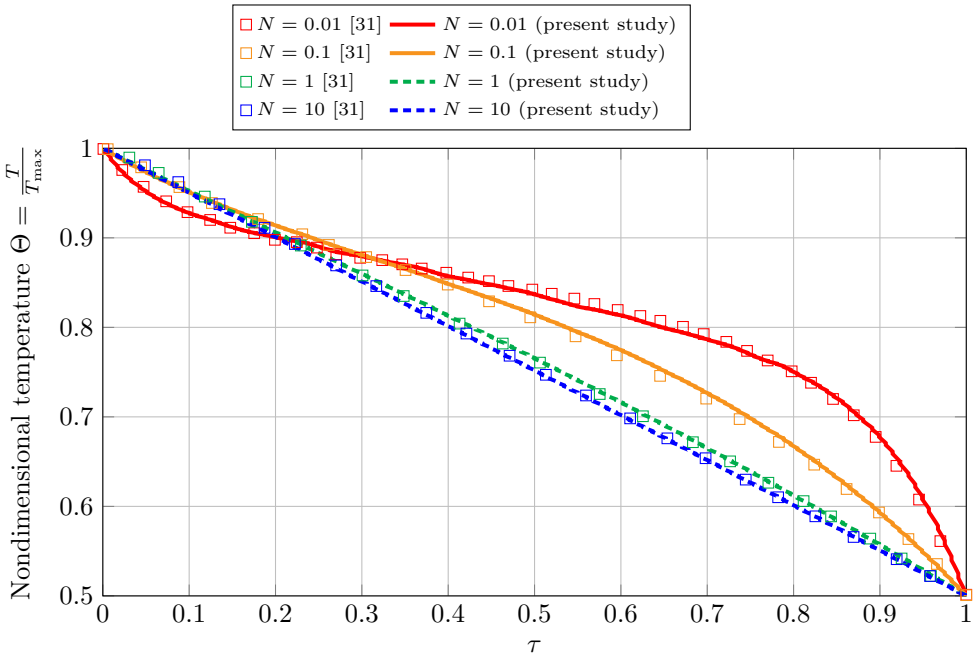

Figure 3: Comparison of our computational results with the results from Viskanta et al. [31] (Fig. 2 Page 68) for different conduction-to-radiation parameters N, (N=0.01, 0.1, 1, 10) with $\Theta_0 = T_{\min}/T_{\max} = 0.5$ ($T_{\max} = 2222.22$ K, $\tau_0 = \kappa L = 1.0$ ($\kappa = 2624.6719$ m^{-1}) and $\sigma = 0$.

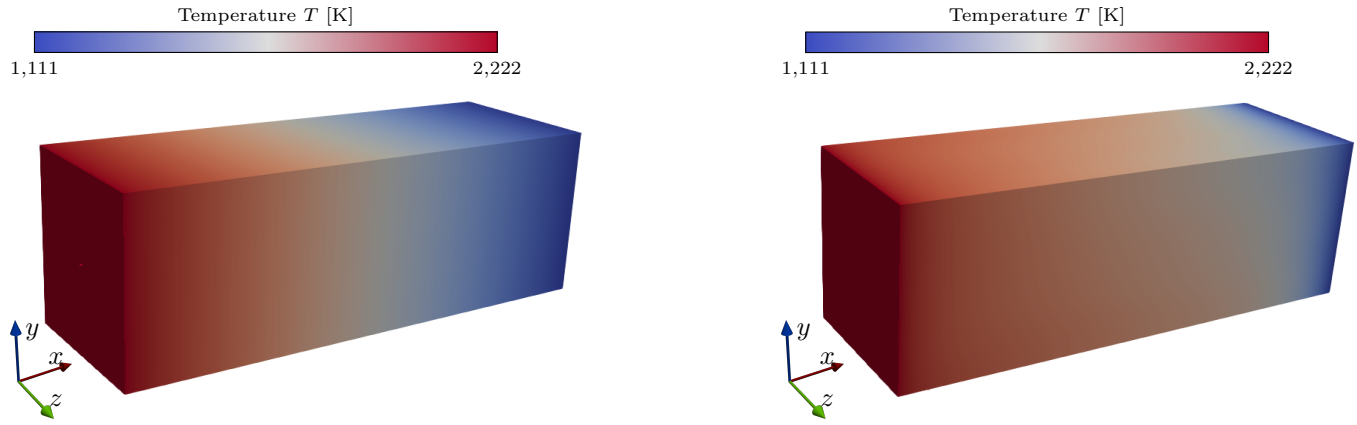

Figure 4: Temperature fields on the three-dimensional domain corresponding to fig. 3, for $N = 10$ (when conduction predominates) on the left, and for $N = 0.01$ (when radiation predominates) on the right.

The validation is performed for several albedos, i.e. ω equal to 0, 0.5, and 1, respectively, and for two temperature ratio θ_0 equal to 0.5 and 0.1, respectively. All the results are summarized in table 2. Figure 5 presents all the corresponding plots in terms of variation of the dimensionless temperature Θ along the main direction of propagation, for different values of ω and Θ_0. In can be seen from presented curves that our three-dimensional results very well coincide with those one-dimensional of Viskanta; this validates completely the numerical modeling of coupled conducto-radiative problem in three-dimensions, with operators of absorption, scattering, emission, and reflection. Please note that other strategies have been developped for validation of the radiative transfer equation only; see our accompanying papers in the references section.

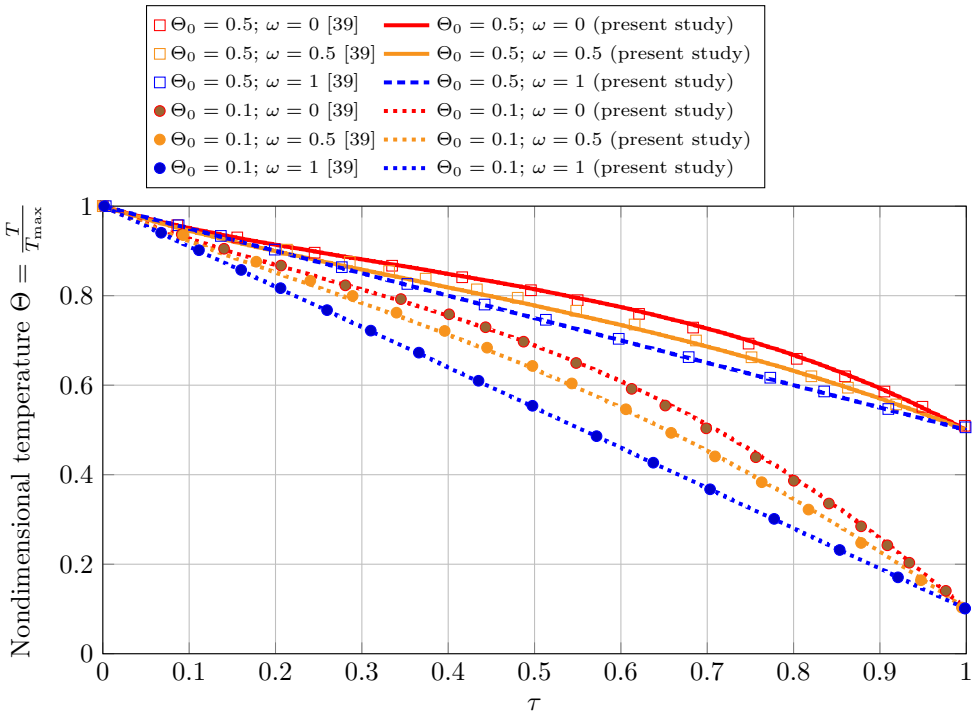

Figure 5: Comparison of our computational results with the results from Viskanta et al. [39] (Fig. 2 Page 146). Effect of scattering albedo on temperature distribution. Conduction-radiation parameter N = 0.1 and $\tau_0 = 1.0$, for $\Theta_0 = 0.5$ and $\Theta_0 = 0.1$.

5.1.2. Convergence analysis

This section presents and discusses convergence results for the three schemes presented in section 3.2.

As a first test case, a scattering medium is considered, with temperature ratio $\theta_0 = 0.1$, albedo $\omega = 0.5$, and Stark number $N = 0.1$. Figure 6 (top-left) shows, for this particular case, the error evolution with respect to the iterations of the inner loop, for the very first iteration of the outer loop (see algorithm 1, line 14). For this particular case, the three iterative schemes are convergent. However, the improved fixed-point method (in orange) converges faster than the ordinary fixed point method (in red), and the Newton-Raphson method (in green) outperforms both fixed-point-type methods. Please note (it is not reported here in plots for the sake of conciseness) that, in all considered cases, when the scheme was convergent, the stabilization was reached after three iterations of the outer loop, at most. We also indicate that the numerical resolution was carried out with the tolerance condition, for both the outer and inner loops, ε^k and ε^l, equal to 10^{-4} (cf. algorithm 1).

As a second test case, a non scattering medium is considered, i.e. $\sigma = 0$, with the Stark number $N = 0.1$. Figure 6 (top-right) shows, for this particular case, the error evolution with respect to the iterations of the inner loop, for the very first iteration of the outer loop. It can be seen that both fixed-point-type methods diverge. The Newton–Raphson method is the only one that converges, and so, very efficiently.

As a third test case, the Rosseland model RM is considered along with $\omega = 0$, $\Theta_0 = 0.5$ and $N = 0.1$. Figure 6 (Bottom-left) shows that the Newton–Raphson method converges much faster than the ordinary fixed point method. Note also that the fixed-point method did not converge for the particular case N=0.01.

As a fourth test case, the discrete-scale coupled model is considered with $\omega_s = 0$, $\Theta_0 = 0.5$ and $N = 0.01$. Figure 6 (Bottom-right) shows, for this particular case, the error evolution with respect to the iterations of the inner loop, for the very first iteration of the outer loop. It can be seen that both fixed-point-type methods diverge; the Newton–Raphson method is the only one that converges, and so, very efficiently.

With the numerical test that we performed, we can also conclude that the computational schemes converge quickly when conduction predominates (the physics is close to being linear), but, when radiation predominates,

the order of convergence is lower (see Figure 7), and the Newton–Raphson method is the only one that gives satisfactory results (see Table 1).

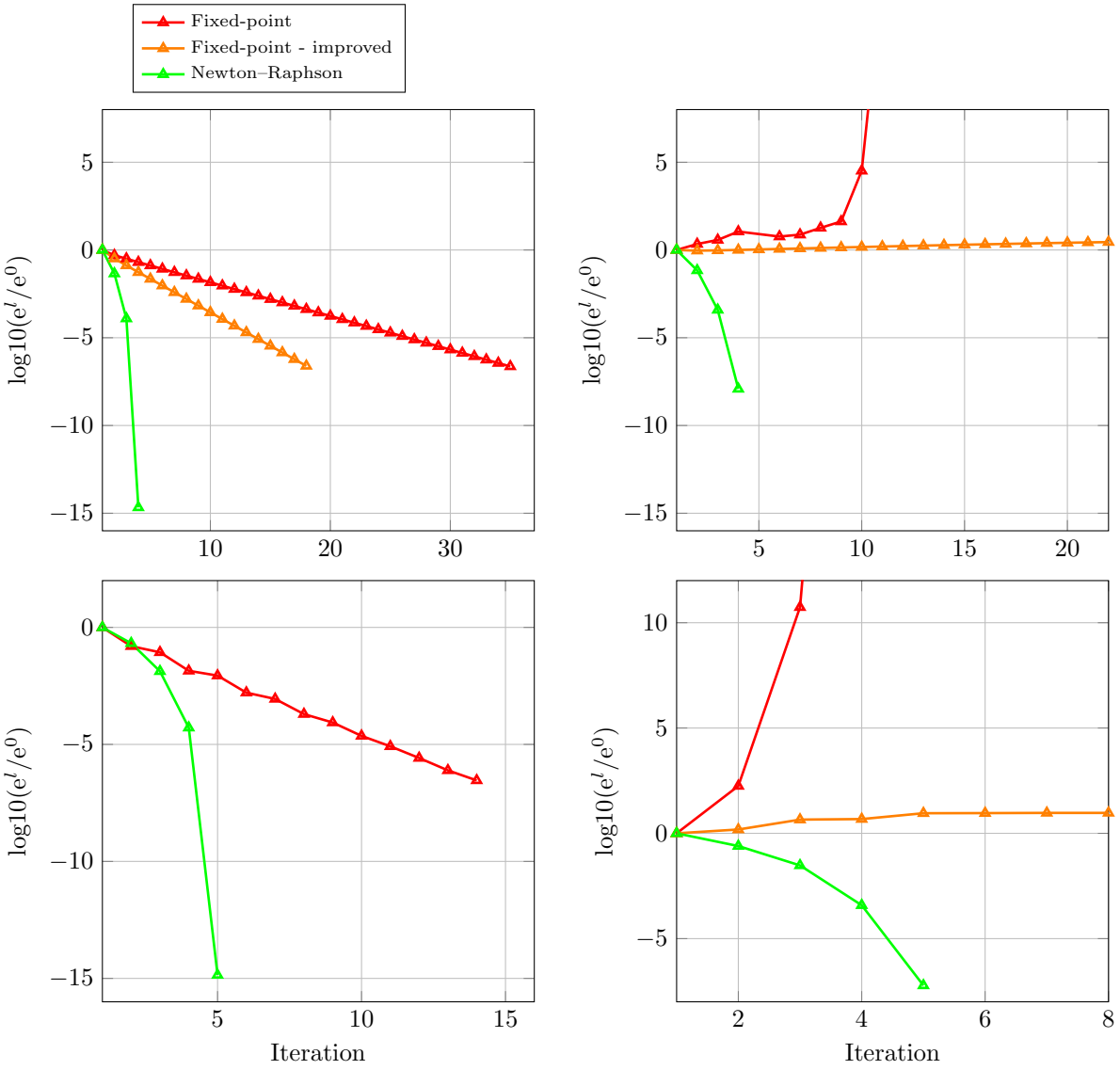

Figure 6: Convergence plots for the three schemes: "ordinary" fixed-point method, "improved" fixed-point method, and Newton–Raphson. Top-left: continuous-scale coupled model CS-CM on a scattering medium ($\omega = 0.5$, $N = 0.1$ and $\Theta_0 = 0.1$). Top-right: continuous-scale coupled model CS-CM on a non-scattering medium ($\omega = 0$, $N = 0.1$ and $\Theta_0 = 0.5$). Bottom-left: Rosseland model RM on a non-scattering medium ($\omega = 0$, $N = 0.1$ and $\Theta_0 = 0.5$). Bottom-right: discrete-scale coupled model DS-CM on a non-scattering medium ($\omega_s = 0$, $N = 0.01$ and $\Theta_0 = 0.5$).

5.1.3. Effect of the anisotropy coefficient

The knowledge at the discrete scale of both the solid-phase conductivity and emissivity, for a given porosity and pore nominal diameter enables us to evaluate both absorption and scattering coefficients of the related effective medium. However, the phase function cannot be determined in such a straightforward way, except using numerical tools such as, for example, the radiation distribution function identification method.

Figure 8 presents on the left the averaged temperature in the continuous-scale effective medium for two very different anisotropy coefficients involved in the Henyey-Greenstein approximation function: $g = -0.9$ for modeling strong backward scattering, and $g = +0.9$ for modeling strong forward scattering. Such curve has been built for two radiation-to-conduction regimes, with the Stark number equal to 0.01, and 0.0001. Figure 8 presents on the right the temperature difference between these both extreme cases and the isotropic scattering case. From this figure, it is seen that the averaged temperature is little sensitive to the anisotropy coefficient (errors are less than 2 %), at least for this considered test case where the effective medium is sandwiched between two given temperatures.

In the whole rest of the study, the anisotropy coefficient has been set to zero yielding isotropic scattering.

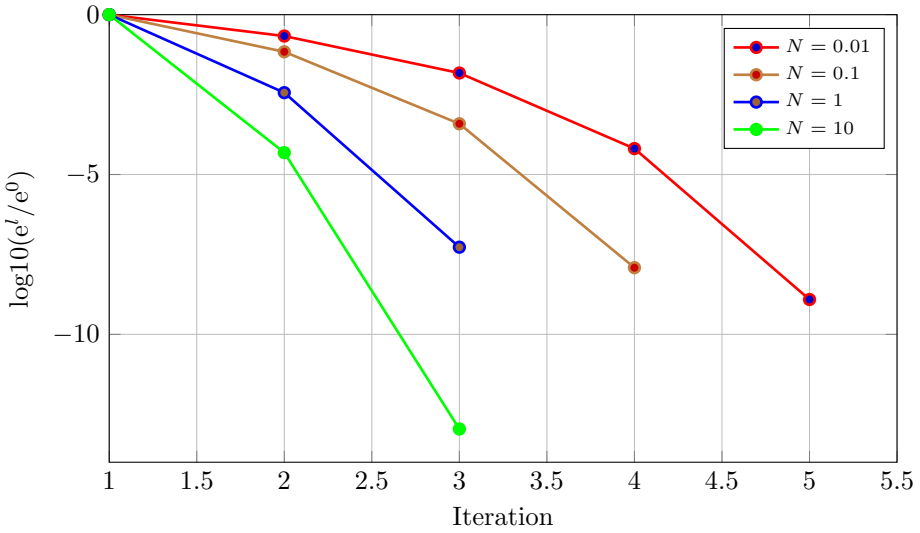

Figure 7: Convergence history of the non-linear heat conduction computational scheme using the Newton-Raphson method for different values of Stark numbers N (from N=10, i.e. when radiation predominates, down to N=0.01, i.e. when conduction predominates) using the CS-CM model and with properties taken from Test A (see Table 2).

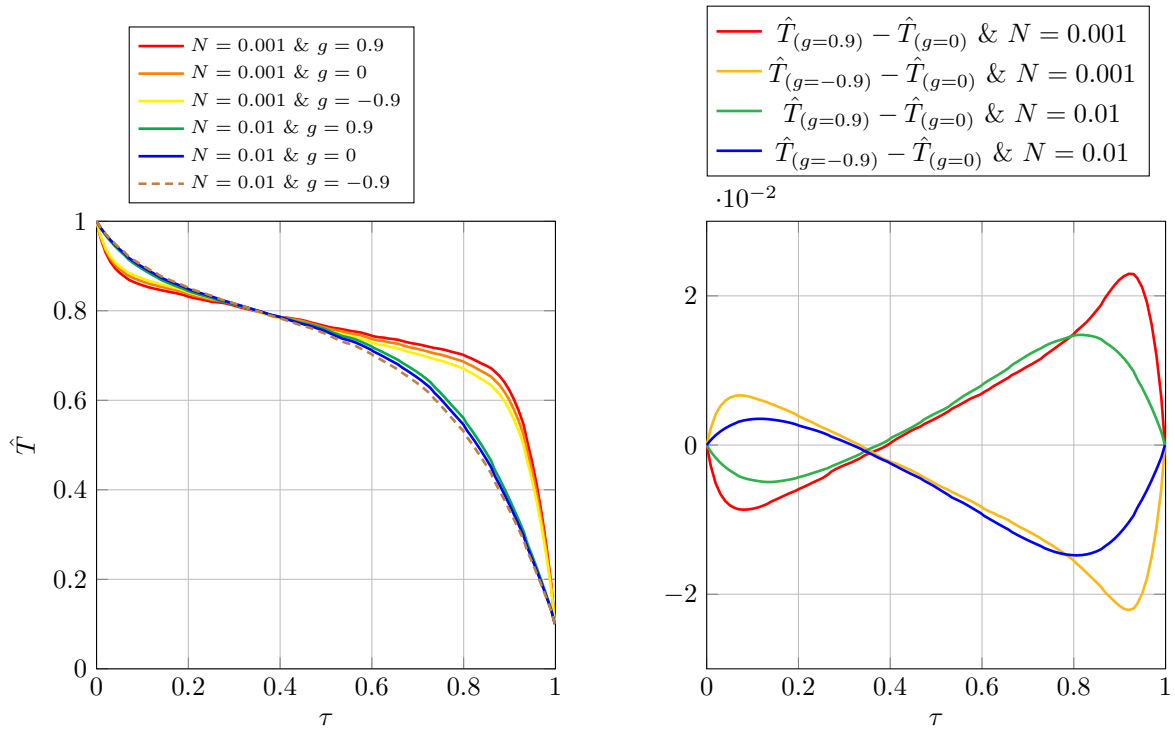

Figure 8: Effect of the anisotropy coefficient on temperature distributions for the continuous-scale coupled model CS-CM using different values of anisotropy coefficients and Stark numbers, with $\{\sigma = 1312,\ \kappa = 1312,\ \theta_0 = 0.1,\ T_{\max} = 2222,$ and $T_{\min} = 222\}$. Left: temperature profiles with $N \in \{0.01; 0.001\}$ and $g \in \{0.9; 0; -0.9\}$. Right: temperature difference for the same values of N.

5.2. Rosseland

The methodology for solving the Rosseland approximation based on finite elements coupled with the Newton–Raphson method is first validated. The method of manufactured solution is used, see for example [40, 12] for other examples in the field of radiation. The manufactured solution is built such that the same Neumann and Dirichlet conditions as that involved in the CS-CM are used. Further, a cubic interpolation has been performed on the CS-CM solution for the case $N = 1$, $\omega = 0$, $\Theta_0 = 0.5$ and $\tau_0 = 10$, yielding a reference solution. All operators involved in the Rosseland model are applied on this reference solution, yielding a source term. Solving the Rosseland model with this source term gives a numerical solution which is to be compared with its reference solution. The comparison is presented in fig. 9-bottom in brown color. As can be seen, the error between the manufactured solution and its reference solution is negligible (in this case the quadratic error is around 0.1 %). This validates numerically the developed methodology based on finite elements and linearization for solving the Rosseland approximation model.

The Rosseland approximation is then compared with respect to the continuous-scale coupled method, in terms of averaged temperature. Three test cases, all recorded in table 2, are used for the comparison. Figure 9 plots the averaged temperature along the e_x axis, as well as the difference with temperature obtained by the CS-CM. Furthermore, table 2 gives errors $\hat{e}_2$, and $\hat{e}_\infty$ between both the Rosseland model and the CS-CM.

A first test case deals with a non-scattering medium, for maximum temperature ratio Θ_0 equal to 0.5, an optical thickness of 1, and for Stark numbers equal to 10, 1, 0.1, and 0.01 (see fig. 9 and table 2, test A). As can be seen, the maximum error is about 5 % at maximum for the case exhibiting high radiation. Other tests, where radiation is less significant, give errors around 1 %.

The following test case (B) deals with errors evolution for different albedos and maximum temperature ratio. As can be seen from table 2 and fig. 9, maximum error is about 10 %. The higher the albedo, the higher the error. Comparing test B-1 and B-2, we conclude that the lower the maximum temperature ratio, the higher the error.

We deduce from these comparisons that the temperature profiles obtained with the Rosseland model tend towards the ones obtained with the continuous-scale couple model when conduction dominates; otherwise, errors become large.

Convergence analysis is also performed on the Rosseland model. The error evolution in terms of iterations is plotted in fig. 6 (bottom-right) for both the ordinary fixed-point method and the Newton–Raphson method, following eq. (33) and eq. (34), respectively. From this figure, both methods converge to the solution, for this particular considered case, and the Newton–Raphson method is more efficient in terms of convergence speed.

5.3. discrete-scale coupled model (DS-CM)

This section presents some coupled conducto-radiative problems similar to those of previous sections, but this time at a discrete scale. The physical properties as well as the discrete geometry have been chosen accordingly to fit with physical properties of the continuous-scale coupled model, following the derivation given in section 4.

In order to perform the immersion of the solid phase within a bounded convex domain representing the void, we consider a cube of size just slightly bigger than L^{Ω_s}.

Firstly, a single cell of the open-cell foam is considered. Then, three and a half cells are considered. Temperature in solid parts as well as radiative density are plotted for both cases, see fig. 10.

For the single-cell case, the geometry as well as physical properties have been set up in such a way that the averaged temperature along the main direction of propagation could be compared with those related to the effective medium. The way this has been done has been explained before in section 4. A quasi-uniform mesh is built for both computational geometries. The mesh size requirement has been set to $h_i = L^{\Omega_s}/80$ for the spatial discretization. This lead to numbers for degrees of freedom equal to ($N_e = 263,931$ tetrahedral elements ; $N_v = 48,731$ vertices) and ($N_e = 1,426,938$ tetrahedral elements ; $N_v = 235,729$ vertices) for the solid and the void, respectively. The number of directions has been set to $N_d = 128$ in order to reach the convergence relatively to the angular discretization. To run such test, 62 processes have been used. Plots of averaged temperature are recorded in fig. 11 for test A (i.e. modifying the Stark number N while keeping null albedo and maximum temperature ratio equal to one half.) and for test B (i.e. modifying the albedo while keeping other quantities of interest constant). From these plots, it is seen that, both CS-CM and DS-CM follow, roughly speaking, the same trend. The main differences between the two models appear close to boundaries where Dirichlet conditions are prescribed. In theses regions, the CS-CM overestimates the temperature gradient. However, the maximum error of the continuous model is about 5 %, and the quadratic error is lower than 1 %.

For the three-cells case, similarly as above, the geometry as well as physical properties have been set up in such a way that the averaged temperature along the main direction of propagation could be compared with those related to the effective medium. A quasi-uniform mesh is built for both computational geometries. The mesh size requirement has been set to $h_i = L^{\Omega_s}/80$ for the spatial discretization. This lead to numbers of degrees of freedom equal to ($N_e = 331,861$ tetrahedral elements ; $N_v = 66,489$ vertices) and ($N_e = 1,753,681$ tetrahedral elements ; $N_v = 289,968$ vertices) for the solid and the void, respectively. The number of directions has been set to $N_d = 128$ in order to reach the convergence relatively to the angular discretization. To run such test, 62 processes have been used. Plots of averaged temperature are recorded in fig. 12 for test A (i.e. modifying the Stark number N while keeping null albedo and maximum temperature ratio equal to one half.), both for the CS-CM and the DS-CM. From these plots, it is seen that, both CS-CM and DS-CM follow the same trend. The main difference between the two models appear close to boundaries where the Dirichlet condition is prescribed (through eqs. (3) and (16)). In the hottest region, the CS-CM slightly overestimates the temperature decrease; the maximum error of the continuous model is about 1 % only.

The same comparison has been performed between the constinuous-scale coupled model and the Rosseland approximation model, see fig. 13. From this plot, it is seen that, both CS-RM and DS-CM roughly speaking follow the same trend, but with large differences. Overall, the temperature is over-estimatated, except in the colder region. Errors are about 5 %, where there were only about 1 % for the continuous-scale coupled model.

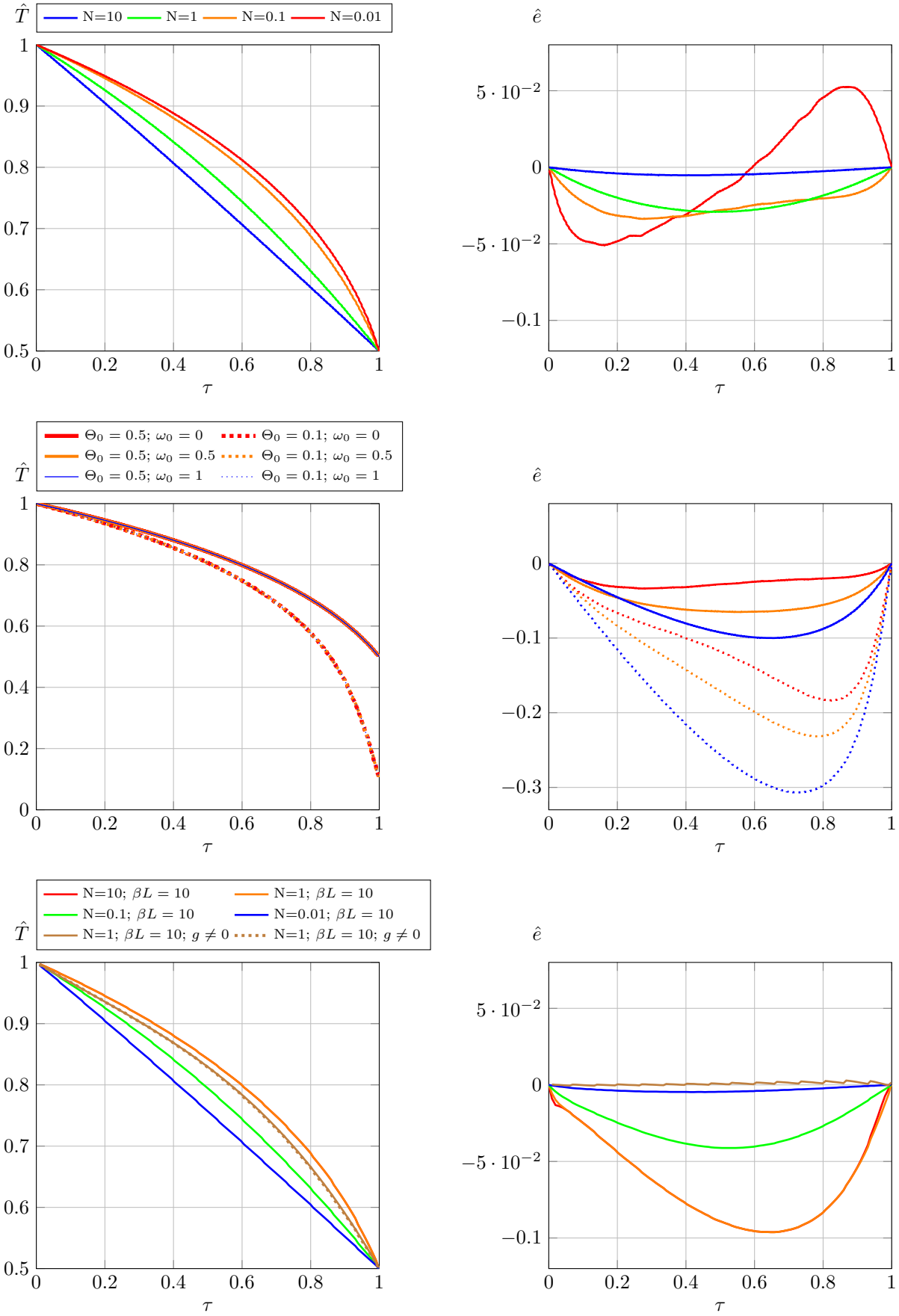

Figure 9: Rosseland model. Left: averaged adimensioned temperature $\hat{T}$ along the axis of propagation x. Right: difference $\hat{e}(x)$ between these temperatures between the Rosseland model and the related continuous-scale coupled model. Top: test A ($N = \{10, 1, 0.1, 0.01\}$, $\omega = 0$, $\Theta_0 = 0.5$, $\tau_0 = 1$). Middle: test B-1 ($N = 0.1$, $\omega = \{0, 0.5, 1\}$, $\Theta_0 = \{0.5, 0.1\}$, $\tau_0 = 1$). Bottom: additional test ($N = \{10, 1, 0.1, 0.01\}$, $\omega = 0$, $\Theta_0 = 0.5$, $\tau_0 = 10$); the brown curves in "line" and "dotted" are respectively the manufactured "exact" and approximate solutions with a non-nul source term g.

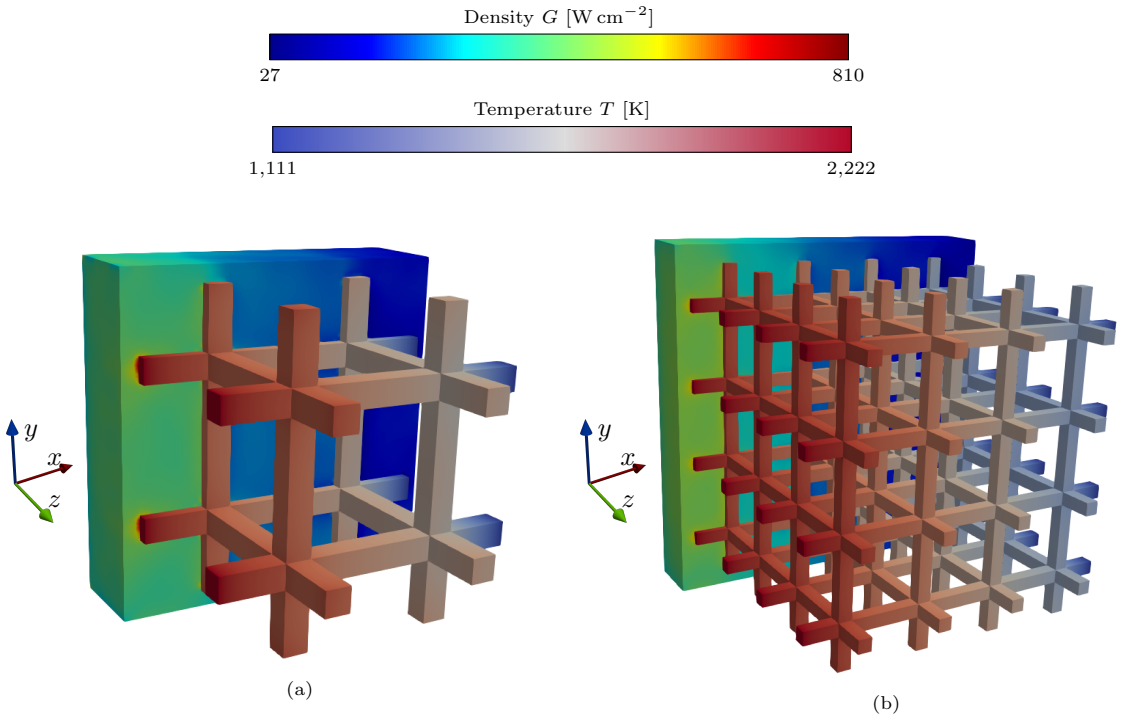

(a) (b)

Figure 10: Radiative density field visualized for the subdomain void part of Ω_v and temperature field visualized for all the solid part Ω_s, for one and three representative elementary volumes, with $N = 0.01$.

5.4. Computation times

Table 1 gives computation costs related to the three models (the discrete-scale couple model, the continuous scale coupled model, and the approximation Rosseland model), for the three numerical schemes (fixed-point method, improved fixed-point method, and Newton–Raphson), for four radiation-to-conduction regimes (for N=10, N=1, N=0.1 nd N=0.01). The computation time takes into account of spatial mesh reading, mesh partitioning, RTE solving, non-linear heat conduction solving, solution writing, etc. From this table, the following conclusions are drawn.

- For any Stark number and for any linearization numerical scheme: the Rosseland model is much cheaper than the continuous-scale coupled model, and the continuous-scale coupled model is much cheaper than the discrete-scale coupled model, but this conclusion is to be balanced with the accuracy of the obtained results discussed above.
- For any Stark number, and for any physical model, when convergence is reached, the Newton–Raphson iterative scheme is more efficient than other fixed-point type methods in terms of computation time. However, the difference time is not much because, for all treated cases, only two outer iterations were necessary (the RTE was solved twice for all cases); while the time difference comes from the number of times the linearized heat conduction equation is solved (see fig. 6), having in mind that the solution of a single iteration of the non-linear heat equation is very small.
- This table eventually shows that, for small Stark numbers (N<0.1), fixed-point type methods may diverge (computation times are set to infinity in Table 1) while the Newton–Raphson linearization scheme is always convergent.

6. Conclusion

The paper compared three distinct conducto-radiative models that can be used for modeling heat transfer at high temperature in view of being integrated within a topology optimization process. Finite elements are extensively used for all models, either using standard Galerkin for the Rosseland approximation as well as for other conduction equations, or in the vectorial form based on the stabilized version of finite elements for the radiative transfer equation. The non-linearity is handled using an iterative scheme. Experiments given here show that the Newton–Raphson strategy converge much faster than other fixed-point type methods.

The considered test case was a three-dimensional square lattice sandwiched between a hot and a cold plate. The model at the discrete level, at the pore scale, was the reference model. For small Stark numbers, when the

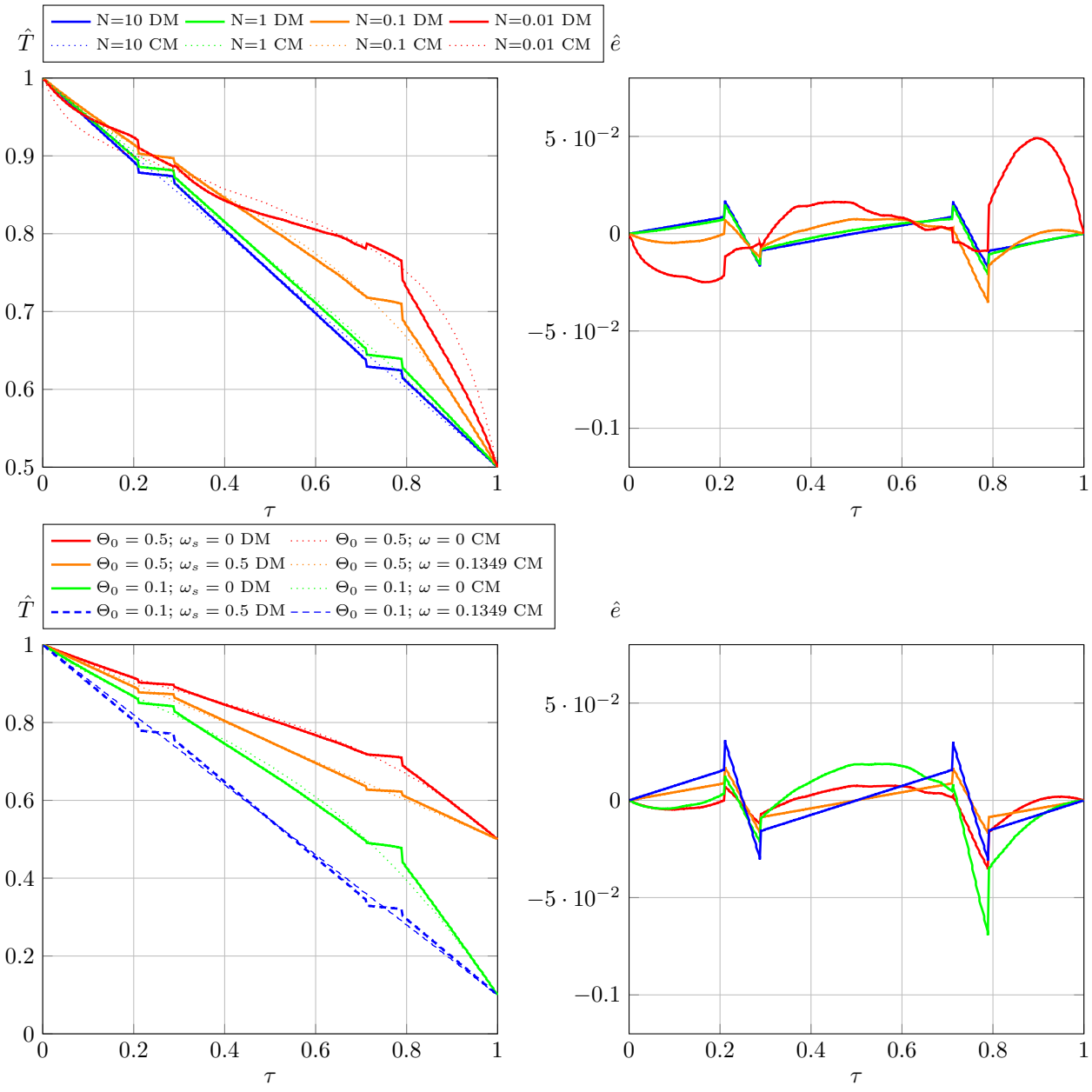

Figure 11: Results of the discrete-scale approche "DM" on the left and its comparison with the continuum-scale approche "CM" on the right ($Val_{CM} - Val_{DM}$); the sub-figures at the top in the case of $\sigma = 0$ for different values of $N \in \{10, 1, 0.1, 0.01\}$ and the sub-figures below in the case of $\sigma \neq 0$ for different values of Θ_0.

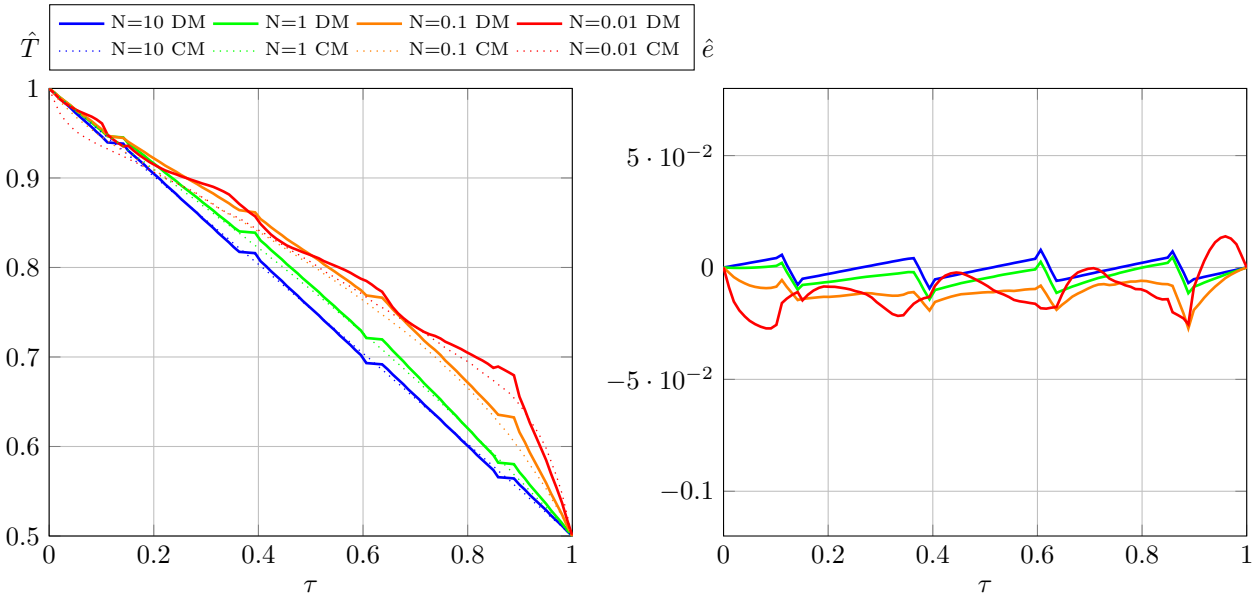

Figure 12: Results of the discrete-scale approach "DM" on the left and its comparison with the continuum-scale approach "CM" on the right ($Val_{CM} - Val_{DM}$); in the porous medium with 3 VER representative elementary volume in each direction and with a porosity of 91 %.

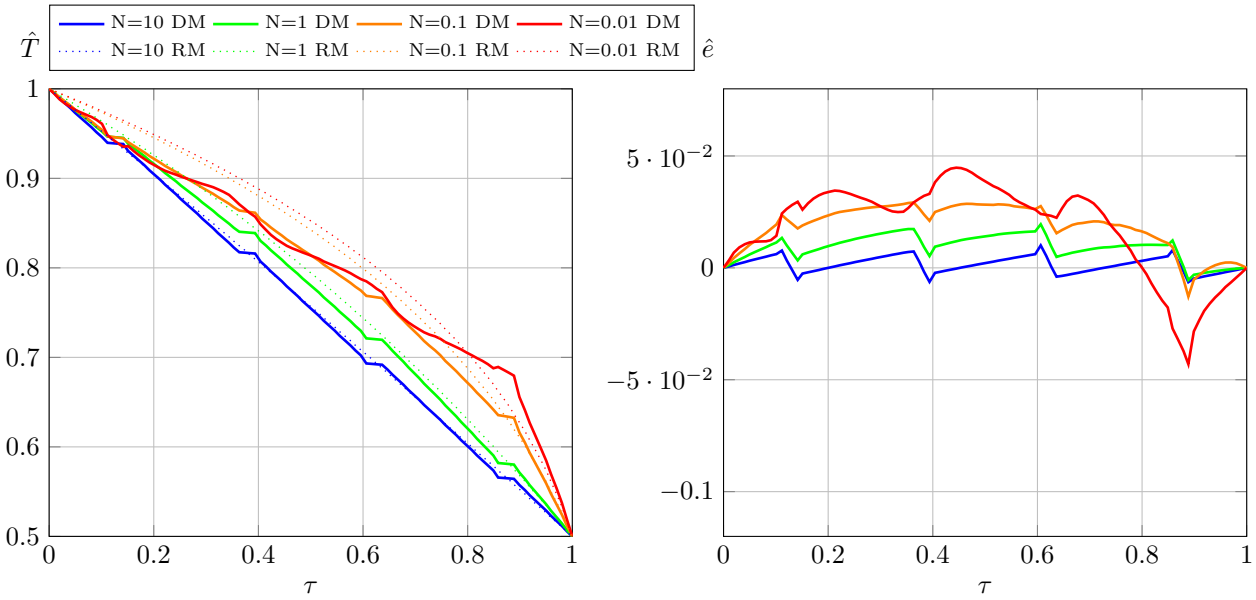

Figure 13: Results of the discrete-scale approach "DM" on the left and its comparison with the continuum-scale approach (Rosseland) "RM" on the right ($Val_{RM} - Val_{DM}$); in the porous medium with 3 VER representative elementary volume in each direction and with a porosity of 91 %.

Model \ Method	N=10			N=1			N=0.1			N=0.01		
	N-R	I F-P	F-P	N-R	I F-P	F-P	N-R	I F-P	F-P	N-R	I F-P	F-P
DS-CM	324 s	336 s	371 s	325 s	339 s	400 s	338	$+\infty$	$+\infty$	347	$+\infty$	$+\infty$
CS-CM	69 s	70 s	70 s	70 s	77 s	78 s	74 s	$+\infty$	$+\infty$	77 s	$+\infty$	$+\infty$
RM	9 s	–	10 s	10 s	–	13 s	11 s	–	17 s	11 s	–	$+\infty$

Table 1: Comparison of the computation costs related to the three models (the discrete-scale couple model – DS-CM, the continuous scale coupled model – CS-CM, and the approximation Rosseland model – RM), for the three numerical schemes (fixed-point method – F-P, improved fixed-point method – I F-P, and Newton–Raphson – N-R), for four radiation-to-conduction regimes (for N=10, N=1, N=0.1 and N=0.01). Values of the Test A of Table 2 have been used, with 62 processes.

conduction-to-radiation parameter is small, i.e. when radiation predominates, it appears that the continuous-scale approach, which has been set-up thanks to proper homogenization laws, gives satisfactory results so that, at most, the error found was about 5 % for a test case involving a single cell. For the case involving $3 \times 3 \times 3$ cells, the maximum error was less, around 1 %. The Rosseland model, because it is very simple and easy to be integrated within an optimizer, has also been tested. This one, however, gives much larger errors: the Rosseland model over-estimates temperature almost everywhere, except in the colder region. The Rosseland model cannot be used confidently within a topology optimization process. The homogenized continuous-scale coupled problem, however, gives satisfactory results and can be used confidently in topology optimization problems.

In the future, some other more complex 3D architectures will be considered. Doing so, relationships of homogenized physical properties, as functions of the textural parameters taken at meso-scale will be consolidated. This will be highly fruitful information for the topology optimization of processes involving conducto-radiative transfers. The main application induced by the presented work is the optimization of architectured materials, and, in particular, lattice materials.

Acknowledgements

The authors would like to thank the FreeFEM team for providing the very efficient finite element library [41]. which has been extensively used in this research. Values used in [31, 39] have been converted into SI units using the online unit converter "https://converter.eu" and, in order to do the comparison, plots have been imported thanks to the open source library PlotDigitizer "http://plotdigitizer.sourceforge.net" [42]. Salih Ouchtout thanks the FEDER and the I-SITE NExT Innovez program for funding its post-doctoral support.

References

[1] M. Pelanconi, S. Zavattoni, L. Cornolti, R. Puragliesi, E. Arrivabeni, L. Ferrari, S. Gianella, M. Barbato, A. Ortona, Application of ceramic lattice structures to design compact, high temperature heat exchangers: material and architecture selection, Materials 14 (2021) 3225.

[2] T. Fend, B. Hoffschmidt, R. Pitz-Paal, O. Reutter, P. Rietbrock, Porous materials as open volumetric solar receivers: Experimental determination of thermophysical and heat transfer properties, Energy 29 (2004) 823–833.

[3] Z. Wu, C. Zhao, Experimental investigations of porous materials in high temperature thermal energy storage systems, Solar Energy 85 (2011) 1371–1380.

[4] R. Capuano, T. Fend, H. Stadler, B. Hoffschmidt, R. Pitz-Paal, Optimized volumetric solar receiver: Thermal performance prediction and experimental validation, Renewable Energy 114 (2017) 556–566.

[5] B. Helber, O. Chazot, A. Hubin, T. E. Magin, Microstructure and gas-surface interaction studies of a low-density carbon-bonded carbon fiber composite in atmospheric entry plasmas, Composites Part A: Applied Science and Manufacturing 72 (2015) 96–107. doi:10.1016/j.compositesa.2015.02.004.

[6] A. Borner, F. Panerai, N. N. Mansour, High temperature permeability of fibrous materials using direct simulation Monte Carlo, International Journal of Heat and Mass Transfer 106 (2017) 1318–1326.

[7] N. Banerji, P. Leyland, S. Haussener, Tomography-based radiative characterisation of decomposing carbonaceous heat shield materials, Carbon (2017) 451–461.

[8] L. Paglia, J. Tirillò, F. Marra, C. Bartuli, A. Simone, T. Valente, G. Pulci, Carbon-phenolic ablative materials for re-entry space vehicles: plasma wind tunnel test and finite element modeling, Materials & Design 90 (2016) 1170–1180.

	Characteristics					Properties				Errors
Test	N	ω/ω_s	Θ_0	τ_0	T_{min}	λ/λ_s	$\varepsilon/\varepsilon_s$	κ	σ	$\begin{pmatrix} e_2^{C-R} & e_2^{R-D} & e_2^{C-D} \\ e_\infty^{C-R} & e_\infty^{R-D} & e_\infty^{C-D} \end{pmatrix}$
A	10	0/0	0.5	1	1111	9.4/323	1/1	2624.67	0	$\begin{pmatrix} 1.4\cdot10^{-5} & 5.2\cdot10^{-5} & 3.7\cdot10^{-5} \\ 5.2\cdot10^{-3} & 2.1\cdot10^{-2} & 1.7\cdot10^{-2} \end{pmatrix}$
	1	0/0	0.5	1	1111	0.94/32.3	1/1	2624.67	0	$\begin{pmatrix} 5.0\cdot10^{-4} & 5.0\cdot10^{-4} & 3.6\cdot10^{-5} \\ 2.9\cdot10^{-2} & 1.9\cdot10^{-2} & 2.1\cdot10^{-2} \end{pmatrix}$
	0.1	0/0	0.5	1	1111	0.094/3.23	1/1	2624.67	0	$\begin{pmatrix} 6.0\cdot10^{-4} & 6.4\cdot10^{-4} & 1.0\cdot10^{-4} \\ 3.3\cdot10^{-2} & 2.2\cdot10^{-2} & 3.5\cdot10^{-2} \end{pmatrix}$
	0.01	0/0	0.5	1	1111	0.0094/0.323	1/1	2624.67	0	$\begin{pmatrix} 1.3\cdot10^{-3} & 8.0\cdot10^{-4} & 4.0\cdot10^{-4} \\ 5.2\cdot10^{-2} & 2.4\cdot10^{-2} & 4.9\cdot10^{-2} \end{pmatrix}$
B-1	0.1	0/0	0.5	1	1111	0.094/3.23	1/1	2624.67	0	$\begin{pmatrix} 6.0\cdot10^{-4} & 6.4\cdot10^{-4} & 1.0\cdot10^{-4} \\ 3.3\cdot10^{-2} & 2.2\cdot10^{-2} & 3.5\cdot10^{-2} \end{pmatrix}$
	0.1	0.13492/0.5	0.5	1	1111	94/3257	0.865/0.5	0.354	0.05	$\begin{pmatrix} 2.7\cdot10^{-7} & 3.8\cdot10^{-5} & 3.7\cdot10^{-5} \\ 7.2\cdot10^{-4} & 1.8\cdot10^{-2} & 1.7\cdot10^{-2} \end{pmatrix}$
	0.1	0.5/-	0.5	1	1111	0.094/-	1/-	1312.235	1312.235	$\begin{pmatrix} 2.6\cdot10^{-3} & - & - \\ 6.5\cdot10^{-2} & - & - \end{pmatrix}$
	0.1	1/-	0.5	1	1111	0.094/-	1/-	0	2624.67	$\begin{pmatrix} 5.2\cdot10^{-3} & - & - \\ 0.1 & - & - \end{pmatrix}$
B-2	0.1	0/0	0.1	1	222.2	0.094/3.23	1/1	2624.67	0	$\begin{pmatrix} 1.4\cdot10^{-2} & 1.4\cdot10^{-2} & 2.6\cdot10^{-4} \\ 0.1 & 1.7\cdot10^{-1} & 6.9\cdot10^{-2} \end{pmatrix}$
	0.1	0.13492/0.5	0.1	1	222.2	94/3257	0.86508/0.5	0.354	0.05	$\begin{pmatrix} 1.0\cdot10^{-6} & 1.2\cdot10^{-4} & 1.0\cdot10^{-3} \\ 1.4\cdot10^{-3} & 3.2\cdot10^{-2} & 3.0\cdot10^{-2} \end{pmatrix}$
	0.1	0.5/-	0.1	1	222.2	0.094/-	1/-	1312.235	1312.235	$\begin{pmatrix} 2.5\cdot10^{-2} & - & - \\ 2.3\cdot10^{-1} & - & - \end{pmatrix}$
	0.1	1/-	0.1	1	222.2	0.094/-	1/-	0	2624.67	$\begin{pmatrix} 4.7\cdot10^{-2} & - & - \\ 3.0\cdot10^{-1} & - & - \end{pmatrix}$

Table 2: Parameters and results of different errors obtained in the comparison of the models CM, RM and DM. Note that: "C", "R" and "D" mean respectively the continuous model, the Rosseland model and the discrete model.

[9] M. Pelanconi, E. Rezaei, A. Ortona, Cellular ceramic architectures produced by hybrid additive manufacturing: A review on the evolution of their design, Journal of the Ceramic Society of Japan 128 (2020) 595–604.

[10] S. Luque, G. Menéndez, M. Roccabruna, J. González-Aguilar, L. Crema, M. Romero, Exploiting volumetric effects in novel additively manufactured open solar receivers, Solar Energy 174 (2018) 342–351.

[11] M. Scheffler, P. Colombo, Cellular ceramics: structure, manufacturing, properties and applications, John Wiley & Sons, 2006.

[12] D. Le Hardy, Y. Favennec, B. Rousseau, Solution of the 2-d steady-state radiative transfer equation in participating media with specular reflections using supg and dg finite elements, Journal of Quantitative Spectroscopy and Radiative Transfer 179 (2016) 149–164.

[13] M. Badri, P. Jolivet, B. Rousseau, S. Le Corre, H. Digonnet, Y. Favennec, Vectorial finite elements for solving the radiative transfer equation, Journal of Quantitative Spectroscopy and Radiative Transfer 212 (2018) 59–74.

[14] M. A. Badri, P. Jolivet, B. Rousseau, Y. Favennec, High performance computation of radiative transfer equation using the finite element method, Journal of Computational Physics 360 (2018) 74–92.

[15] P. Jolivet, M. A. Badri, Y. Favennec, Deterministic radiative transfer equation solver on unstructured tetrahedral meshes: Efficient assembly and preconditioning, Journal of Computational Physics 437 (2021) 110313.

[16] M. A. Badri, P. Jolivet, B. Rousseau, Y. Favennec, Preconditioned Krylov subspace methods for solving radiative transfer problems with scattering and reflection, Computers & Mathematics with Applications 77 (2019) 1453–1467.

[17] D. Le Hardy, Y. Favennec, B. Rousseau, F. Hecht, Specular reflection treatment for the 3d radiative transfer equation solved with the discrete ordinates method, Journal of Computational Physics 334 (2017) 541–572.

[18] Y. Favennec, T. Mathew, M. A. Badri, P. Jolivet, B. Rousseau, D. Lemonnier, P. J. Coelho, Ad hoc angular discretization of the radiative transfer equation, Journal of Quantitative Spectroscopy and Radiative Transfer 225 (2019) 301–318.

[19] M. Badri, Y. Favennec, P. Jolivet, B. Rousseau, Conductive-radiative heat transfer within sic-based cellular ceramics at high-temperatures: A discrete-scale finite element analysis, Finite Elements in Analysis and Design 178 (2020) 103410.

[20] D. Y. Perraudin, S. Haussener, Numerical quantification of coupling effects for radiation-conduction heat transfer in participating macroporous media: Investigation of a model geometry, International Journal of Heat and Mass Transfer 112 (2017) 387–400.

[21] M. F. Modest, S. Mazumder, Radiative heat transfer, Academic press, 2021.

[22] J. R. Howell, M. P. Mengüç, K. Daun, R. Siegel, Thermal radiation heat transfer, CRC press, 2020.

[23] D. Baillis, J.-F. Sacadura, Thermal radiation properties of dispersed media: theoretical prediction and experimental characterization, in: Radiative Transfer II. Proceedings of the Second International Symposium on Radiation Transfer, Begel House Inc., 1997.

[24] J. Taine, F. Bellet, V. Leroy, E. Iacona, Generalized radiative transfer equation for porous medium upscaling: Application to the radiative fourier law, International Journal of Heat and Mass Transfer 53 (2010) 4071–4081.

[25] M. Tancrez, J. Taine, Direct identification of absorption and scattering coefficients and phase function of a porous medium by a monte carlo technique, International Journal of Heat and Mass Transfer 47 (2004) 373–383.

[26] F. Bellet, E. Chalopin, F. Fichot, E. Iacona, J. Taine, Rdfi determination of anisotropic and scattering dependent radiative conductivity tensors in porous media: Application to rod bundles, International Journal of Heat and Mass Transfer 52 (2009) 1544–1551.

[27] P. Comninos, Mathematical and Computer Programming Techniques for Computer Graphics, Springer, 2006.

[28] M. Sans, Caractérisation des propriétés thermophysiques de mousses céramiques à haute température, Ph.D. thesis, Université de Lorraine, 2019.

[29] H. Brezis, H. Brézis, Functional analysis, Sobolev spaces and partial differential equations, volume 2, Springer, 2011.

[30] D. T. Whiteside, The mathematical papers of Isaac Newton, volume 1982, Cambridge University Press Cambridge, 1967.

[31] R. Viskanta, R. Grosh, Heat transfer by simultaneous conduction and radiation in an absorbing medium (1962).

[32] S. Guévelou, B. Rousseau, G. Domingues, J. Vicente, A simple expression for the normal spectral emittance of open-cell foams composed of optically thick and smooth struts, Journal of Quantitative Spectroscopy and Radiative Transfer 189 (2017) 329–338.

[33] A. Kribus, Y. Gray, M. Grijnevich, G. Mittelman, S. Mey-Cloutier, C. Caliot, The promise and challenge of solar volumetric absorbers, Solar Energy 110 (2014) 463–481.

[34] R. S. Murray, mathematical handbook of formulas and tabel, 2009.

[35] T. Le, C. Moyne, M. Sans, Homogenized models of conduction-advection-radiation heat transfer in porous media, International Journal of Heat and Mass Transfer 194 (2022) 123056.

[36] T. Hendricks, J. Howell, Absorption/scattering coefficients and scattering phase functions in reticulated porous ceramics (1996).

[37] S. Guévelou, B. Rousseau, G. Domingues, J. Vicente, C. Caliot, Representative elementary volumes required to characterize the normal spectral emittance of silicon carbide foams used as volumetric solar absorbers, International Journal of Heat and Mass Transfer 93 (2016) 118–129.

[38] K. Kamiuto, Modeling of composite heat transfer in open-cellular porous materials at high temperatures, Cellular and Porous Materials: Thermal Properties Simulation and Prediction (2008) 165–198.

[39] R. Viskanta, Heat transfer by conduction and radiation in absorbing and scattering materials (1965).

[40] H. Gao, H. Zhao, A fast-forward solver of radiative transfer equation, Transport Theory and Statistical Physics 38 (2009) 149–192.

[41] F. Hecht, New development in freefem++, Journal of Numerical Mathematics 20 (2012) 251–266.

[42] J. A. Huwaldt, S. Steinhorst, Plot digitizer, URL http://plotdigitizer. sourceforge. net (2013).